CANTILEVER-BASED RF- MEMS SWITCHES FOR 5G APPLICATIONS

by

HEBA SALEH

Submitted to the Graduate School of Engineering and Natural Sciences

in partial fulfilment of

the requirements for the degree of Master of Science

Sabancı University

June 2022

HEBA SALEH 2022 ©

All Rights Reserved

ABSTRACT

CANTILEVER-BASED RF-MEMS SWITCHES FOR 5G APPLICATIONS

HEBA SALEH

ELECTRONICS ENGINEERING M.Sc. THESIS, JUNE 2022

Thesis Supervisor: Asst. Prof. Dr. Murat Kaya Yapici

Keywords: RF-MEMS switch; shunt switch; low actuation voltage; 5G; cantilever; switch design; finite element modeling; pull-in; mechanical reliability; von Mises stress; stiction; electromechanical-RF optimization.

Fifth-generation (5G) mobile communications are developed for Internet of Things (IoT) applications such as industrial automation, cloud robots, and safety-critical vehicle communications. The emerging 5G requires fast data rates, minimal latency, and wide coverage. In order to fulfill these demands improved slot-based architecture, mm-wave bands, and beamforming are being designed. These technologies require RF front-end switches with high isolation, frequency filtering, low insertion loss, high linearity, and fast switching. This thesis studies cantilever-based RF-MEMS switch performance at high frequencies for 5G applications. The RF-MEMS switch is first designed in a series configuration and exploits intrinsic stresses within a thin film to build a self-assembled cantilever beam based on bi-directional control of intrinsic stresses to reconstruct straight cantilever beams into out-of-plane wavy structures. The novel switch design displays a low insertion loss of -0.5 dB in the on-state and high RF isolation of -22 dB in the off-state at 30 GHz due to the large air gap between the distal end of the cantilever switch (RF_{in}) and underlying contact pad (RF_{out}), while maintaining a low operation voltage of 10.5 V. In addition, to reduce the inherent high actuation voltage needs of conventional electrostatic fixed–fixed shunt switches, a cantilever-based RF-MEMS switch with a shunt configuration has also been designed and, systematically optimized both from electromechanical and RF performance aspects achieving a pull-in voltage of 9 V, low insertion loss of -0.14 dB, and high isolation of -44.7 dB at 30 GHz. The novel cantilever-based series and shunt RF-MEMS switches designed in this thesis exhibit low insertion losses, high isolation and low pull-in voltages, making them ideal for 5G mobile applications.

ÖZET

5G UYGULAMALARI İÇİN KONSOL TABANLI RF-MEMS ANAHTARLARI

HEBA SALEH

ELEKTRONİK MÜHENDİSLİĞİ YÜKSEK LİSANS TEZİ, HAZİRAN, 2022

Tez Danışmanı: Dr. Öğr. Üyesi Murat Kaya Yapıcı

Anahtar Kelimeler: RF-MEMS switch; shunt switch; low actuation voltage; 5G; cantilever; switch design; finite element modeling; pull-in; mechanical reliability; von Mises stress; stiction; electromechanical-RF optimization.

Beşinci nesil (5G) telekomünikasyonun farklı nesnelerin interneti (IoT) uygulamalarında kullanılması hedeflenmektedir. Endüstriyel otomasyon, bulut robotları ve güvenlik açısından kritik araç iletişimleri bu uygulama alanlarından sadece bazılarıdır. Hızla gelişmekte olan 5G haberleşmede yüksek veri hızı, minimum gecikme süresi ve geniş kapsama alanı kritiktir. Bu talepleri karşılamak için iyileştirilmiş yuva tabanlı mimari, mm dalga bantları ve hüzmelemeye dayalı çözümler geliştirilmektedir. Kullanılan RF ön yüz anahtarlanın da yüksek izolasyon, frekans filtreleme, minimum giriş kaybı, yüksek doğrusallık ve hızlı anahtarlama gerekliliklerini karşılaması gerekir. Bu tez, 5G uygulamaları için geliştirilen bir yüksek frekans RF-MEMS anahtarını sunmaktadır. İlk olarak RF-MEMS anahtarları seri bir konfigürasyonda tasarlanmış ve kendiliğinden düzenlenen bir kiriş (manivela) elde edilmesi amacıyla ince film içsel gerilimlerden yararlanılmıştır. Böylelikle alışılagelmiş doğrusal kirişler yerine, düzlem dışı dalgalı yapılar elde edilebilmiştir. Yeni anahtar tasarımı, açık durumda -0.5 dB'lik düşük bir ekleme kaybı ve kapalı durumda da konsol anahtarının (Rfin) uzak ucu ile alttaki temas pedi (Rfout) arasındaki büyük hava boşluğu sayesinde 30 GHz'de -22 dB'lik yüksek RF izolasyonu sağlarken, 10,5 V'luk düşük bir tahrik gerilimine sahiptir. Ek olarak, geleneksel elektrostatik sabit-sabit anahtarların doğasında bulunan yüksek tahrik gerilimi ihtiyaçlarını azaltmak için paralel konfigürasyonlu (şönt) manivela tabanlı bir RF-MEMS anahtarı da geliştirilmiş olup,t elektromekanik ve RF performansı yönünden yapılan sistematik optimizasyon ile 9 V'luk bir çekme voltajı, -0.14 dB'lik düşük ekleme kaybı ve 30 GHz'de -44.7 dB'lik yüksek izolasyon elde edilmiştir. Bu tez kapsamında tasarlanan manivela-tabanlı seri ve şönt anahtarların sergilediği düşük ekleme kaybı, yüksek izolasyon ve düşük çekme gerilimi , söz konusu anahtarları5G mobil uygulamalar için elverişli kılmaktadır.

ACKNOWLEDGEMENTS

I would like to express my gratitude to all those who helped me all these years through graduate school. Without them, would have not been possible.

I would like to express my deepest appreciation and thanks to my advisor Professor Murat Kaya Yapıcı, I would like to thank you for encouraging my research and for allowing me to grow as a research scientist. Your advice on all aspects of life has been precious. I would also like to thank my committee members, Professor İbrahim Tekin and Professor Dooyoung Hah for serving as my committee members.

It was a great pleasure for me to work in the SU-MEMS Labs with so many talented individuals. I would not be able to accomplish this without the help and mentorship of my colleagues Rayan Bajwa and Milad Shojaeian.

Additionally, I would like to acknowledge that this work was supported in part by the Scientific and Technological Research Council of Turkey (TUBITAK), Grant No: 118E842.

Finally, I would like to acknowledge with gratitude, the support and love of my family-parents, my brother, and my sisters. They all kept me going and sustained me thus far.

Last but not least nobody has been more important to me in the pursuit of this thesis than my husband, Habib Mousa. I would like to thank him, whose love and guidance are with me in whatever I pursue. Without you, it would have been impossible for me to achieve this. Thank you!

TABLE OF CONTENTS

ABSTRACT ... iv

ÖZET. ... v

ACKNOWLEDGEMENTS ... vi

LIST OF TABLES ... x

LIST OF FIGURES ... xi

LIST OF EQUATIONS ... xiv

LIST OF ABBREVIATIONS ... xv

I. INTRODUCTION ... 1

1.1. RF-MEMS Switches And Their Applications ... 2

1.2. Types of RF Switches ... 4

1.3. Motivation ... 6

1.4. Thesis Structure ... 7

II. DEVELOPMENT OF ELECTROSTATIC RF-MEMS SWITCHES ... 10

2.1. Actuation Voltage, Displacement, And Restoring Forced ... 10

2.2. Adhesion Between Actuation Electrodes ... 13

2.3. Material ... 13

2.4. Residual Stress And Stress Gradient Tolerance ... 14

2.5. Contact Area Verses RF Performance ... 15

2.6. Effect Of Up State Coupling Capacitance On RF Performance ... 17

2.7. Substrate And Transmission Line ... 17

III. DESIGN AND MODELING OF CANTILEVER TYPE RF-MEMS SWITCHES 18

3.1. Wavy Cantilever RF-MEMS Switch Design 19
3.1.1. The Switch Concepts 19
3.1.2. Switch Design 23
3.1.3. Electrical and Mechanical Simulation of the RF Switch 25
3.2. Cantilever Based Capacitive RF-MEMS Shunt Switch Design 28
3.2.1. The Switch Concepts 28
3.2.2. Switch Design 30
3.2.3. Electrical and Mechanical Simulation of the RF Switch 32
IV. PROCESS FLOW FOR FABRICATION OF CANTILEVER-TYPE RF-MEMS SWITCHES 40
4.1. Overview of the process flow 41
4.2. Cleaning of the Glass Substrate 42
4.3. Layer 1: Deposition Of Polysilicon For DC Bias Line And electrode 42
4.4. Layer 2: Deposition Of Silicon Dioxide Intermetal Dielectric Between The DC Bias Line And CPW 43
4.5. Layer 3: Metallization To Define The Transmission Line.............................. 44
4.6. Layer 4: Deposition Of The Sacrificial Layer Deposition And Patterning Of The Beam's Anchor 46
4.7. Layer 5: Metallization To Form The Cantilever 49
4.8. Removal of the Sacrificial Layer 50
V. RESULTS AND DISCUSSION 51
5.1. Wavy Cantilever RF-MEMS Switch Characterization 51
5.1.1. RF Characterization of the RF Switch 51
5.1.2. Mechanical Characterization of the RF Switch 53
VI. CONCLUSION AND FUTURE WORK 54
VII. REFERENCE.. 56
APPENDIX A RF-MEMS Switch on High Resistive Silicon Substrate Simulations.. 61

APPENDIX B RF-MEMS Switch on Glass Substrate With Copper DC Biasing Electrode Simulations 63

APPENDIX C Cantilever Based Capacitive RF-MEMS Shunt Switch Design process flow fabrication and Results 64

APPENDIX D Mask layouts used in RF-MEMS Switch Fabrication.......................... 66

APPENDIX E A5214E Photolithography Recipes 70

LIST OF TABLES

Table 1.1 MEMS switches benefits and drawbacks 3
Table 2.1 A literature review summary 11
Table 3.1 Advantages of series and shunt topologies 19
Table 3.2 RF-MEMS switch in series configuration 20
Table 3.3 performance comparison of different simulation literature 28
Table 3.4 Structural Elements and Geometry of the Switch... 32
Table 3.5 Performance comparison with simulation-based studies in literature 39
Table 4.1 PECVD Parameters settings 43
Table 4.2 The results for different materials used as sacrificial layer 47
Table 4.3 Sputtering process parameters 49
Table E.1 Positive photolithography recipe……………………………………………...70
Table E.2 Image reversal photolithography recipe…………………………………...…70

LIST OF FIGURES

Figure 1.1 RF-MEMS switch Classification 5
Figure 1.2 Cross-section view for series switches with DC metal contacts with electrostatic actuation. 6
Figure 1.3 Cross-section view for Capacitive shunt switches with electrostatic actuation. 6
Figure 1.4 Analytical approach to develop the proposed RF-MEMS Switches. 8
Figure 2.1 A simple spring-based switch representative (a) electromechanical equivalent circuit (b) active forces on the beam. 11
Figure 2.2 The interconnection between the design parameters that affects the contact performance. 16
Figure 3.1 Schematic diagram showing the induced bending in bilayer thin-film system when subjected to residual tensile stresses. The stresses σ1 and σ2 are the misfit stresses in the Cr and Cu. 21
Figure 3.2 Bending profile for varying cantilever lengths and fabricated at three different film thicknesses [57]. 22
Figure 3.3 Wavy Cantilever RF-MEMS Switch based on Bidirectional Control of Intrinsic Stress 23
Figure 3.4 Top view of the proposed Series RF-MEMS switch. 24
Figure 3.5 bending profile of wavy switch cantilever. 26
Figure 3.6 Tip displacement vs applied DC actuation voltage. 26
Figure 3.7 performance against the switch's geometrical parameters (a) Down switch position (ON-state), (b) up switch position (OFF-state). 27
Figure 3.8 Simulated S-parameters of wavy RF-MEMS switch in the (a) ON-state and (b) OFF-state position with Vpull-in = 40 V. 28
Figure 3.9 Cross-sectional view for the proposed cantilever-based RF-MEMS shunt switch. 30
Figure 3.10 the proposed cantilever-based shunt RF-MEMS switch 31
Figure 3.11 Schematic view of the RF switches: (a) Case 1, a simple cantilever; (b) Case 2, a non-uniform cantilever; (c) Case 3, a non-uniform cantilever with square perforations. 33

Figure 3.12 Normalized tip deflection vs applied DC actuation voltage........................ 34
Figure 3.13 Time-dependent response for the three selected designs of the proposed switch.. 35
Figure 3.14 (a) Plot of the maximum stress value during actuation for the three cases. Stress contour plots for: (b) Case 1; (c) Case 2, and (d) Case 3. 36
Figure 3.15 Simulated insertion loss against frequency for the proposed switch........... 37
Figure 3.16 Simulated return loss against frequency for the proposed switch. 38
Figure 3.17 Simulated RF isolation against frequency for the proposed switch. 38
Figure 4.1 Standard MEMS fabrication processes. 40
Figure 4.2 The proposed RF-MEMS Switch process flow.. 42
Figure 4.3 Patterning of CPW using (a) wet etching and Liftoff. 44
Figure 4.4 Liftoff process (a) After reverse image step before deposition (b) after removing the underneath photoresist.. 45
Figure 4.5 The before and after results of the optimized metal deposition. 46
Figure 4.6 SEM and optical images for the results obtained corresponding to different materials used as the sacrificial layer. 48
Figure 4.7 Final deposition of the cantilever beam layer. 50
Figure 4.8 SEM images of Wavy MEMS switches. 50
Figure 0.1 Measured S-parameters for the proposed wavy RF-MEMS switch (OFF-state) isolation and (ON-state) insertion loss……………………………………………54
Figure 0.2 On/Off operation performed with fabricated wavy switch…………………..55
Figure A.1 Simulated S-parameters of wavy RF-MEMS switch on high resistive silicon in the (a) ON-state and (b) OFF-state position…………………………………………… 63
Figure A.2 Simulated insertion loss against frequency for the proposed Cantilever Based Capacitive RF-MEMS Shunt switch on high resistive silicon……………………63
Figure A.3 Simulated return loss against frequency for the proposed Cantilever Based Capacitive RF-MEMS Shunt switch on high resistive silicon……………………………64
Figure A.4 Simulated isolation against frequency for the proposed Cantilever Based Capacitive RF-MEMS Shunt switch on high resistive silicon……………………………64
Figure B.1 Simulated S-parameters of wavy RF-MEMS switch on glass substrate using copper biasing electrode in the (a) ON-state and (b) OFF-state position………………..65
Figure C.1 The proposed cantilever based capacitive RF-MEMS shunt switch process flow……………………………………………………………………………………..66
Figure C.2 The deflection of the shunt cantilever RF-MEMS switch……………………67
Figure D.1 Mask 1 DC pad and electrode pattern…………………………………………68

Figure D.2 Mask 2 DC pad pattern to remove oxide layer above DC contact………….69

Figure D.3 Mask 3 CPW pattern………………………………………………………….70

Figure D.4 Mask 4 anchor pattern……………………………………….………….…..70

Figure D.5 Mask 5,6 & 7 tri-layer beam patterns……………………………………….71

LIST OF EQUATIONS

Equation 2.1 Pull-in voltage equation……………………………………………………..…11

Equation 2.2 Loss equation…………..……………………………………………………..…15

Equation 2.3 Simplified loss equation……………………………………………….……...15

Equation 2.4 Ohmic cantilever resistance equation…………………………………..…15

Equation 2.5 Down-state shunt capacitance equation…………….….……………………17

Equation 2.6 Up-state Capacitance equation…..……...……………………………………..…17

Equation 3.1 Up-state shunt Capacitance equation ……………………………………..…30

Equation 3.2 Shunt Capacitance ratio equation …...……………………………………..…31

LIST OF ABBREVIATIONS

MEMS Micro-electro-mechanical systems 1

IC Integrated circuits..1

RF-MEMS Radio-frequency microelectromechanical systems..1

SSR Solid-state relays..1

5G fifth-generation..3

IoT Internet of Things 3

ATE Automatic test equipment 3

Cu Copper 14

Au Gold 14

HR-Si Highly resistive silicon 18

SOI Silicon-on-insulator 18

CPW Coplanar waveguide 18

FEM Finite element modeling 19

Cr Chromium 21

CMOS Complementary metal oxide semiconductor 39

CVD Chemical vapor deposition 39

PVD Physical vapor deposition 39

DRIE Deep reactive ion etching 39

PECVD Plasma enhanced chemical vapor deposition 40

IPA Isopropanol 41

N_2 Nitrogen 41

DI Deionized water 41

HMDS Hexamethydisilazine 43

IR Image reversal mode 43

VNA Vector Network Analyzer 49

GSG ground–signal–ground 50

I. INTRODUCTION

Micro-electro-mechanical systems (MEMS) are integrated microdevices that combine electrics with passive and active interaction characteristics with their physical parameters. They interact with movement, sound, light, radio waves, gases, liquids, chemical reactions, and heat transfer, among other things. The enormous promise of MEMS lies in their capacity through increasing their scalability and efficiency by using fabrication processes from a proven and optimized traditional semiconductor, infrastructure, and logistics. MEMS devices are fabricated in a method similar to that of integrated circuits (IC) and numerous applications have been developed for MEMS devices such as accelerometers, pressure sensors, temperature sensors, biosensors, and radio-frequency microelectromechanical systems (RF MEMS) devices.

RF-MEMS are micromachined devices that interact with electrical impulses in the radio frequency band. They are believed to have the greatest commercial potential, given there is currently a substantial consumer market for communication devices. Particularly, relays are a common component in RF-MEMS applications. Especially, miniaturized mechanical relays outperform their electronic equivalents, solid-state relays (SSR), in terms of cost, isolation, and on-resistance. Due to the requirement for significant downsizing, it is critical to develop a device that bridges the technological and economic gap between electromechanical "macro-relays" and solid-state devices for commercial demand [1]. The MEMS technology enables economies of scale, precision, and device customization. As a result, micromachining appears to be a viable technology for fabricating ultra-compact, low-cost micromechanical relays [2].

In essence, RF-MEMS switches are used to mechanically open or close a transmission line. Currently, universities, research institutes, and businesses are all closely monitoring the performance of RF-MEMS switches, due to the continued demand for enhanced signal switching characteristics in increasingly complex telecommunications standards and high-end applications [2, 3].

1.1. RF-MEMS Switches And Their Applications

A RF-MEMS switch is a bi-state mechanical device created using microfabrication techniques that allows RF signal to propagate freely between an input and an output in one state and filters the signal in the other. Hence, stabilization in both states can be attained with or without the use of external power force, which means the transition between the two states can be regulated by applying or releasing external effort.

MEMS switches work effectively over an exceptionally wide bandwidth with remarkably consistent properties, even at frequencies beyond 100 GHz [3]. That is the benefit of using a purely mechanical device to open and close or short circuit otherwise unaltered transmission line. Even though, MEMS switches are gaining a lot of interest MEMS switches do have some downsides. In particular, a DC metal contact switch is a mechanically challenging and sophisticated device when compared to other conventional MEMS devices.

Despite the disadvantages displayed in table 1.1, such as a low switching speed (1–100 s) and a lower power handling capabilities (1–2 W) when compared to modern solid-state, they exhibit remarkable performance such as [2]:

1. Low Insertion Loss; based on the conductivity of the metal used for the switching beam and transmission line, RF-MEMS switches have a very low loss of roughly 0.05–0.5 dB from DC–100 GHz.

2. Low power demand: Whereas the MEMS switch involves a high actuation voltage (20–100 V), its current consumption is minimal, resulting in decreased DC power dissipation.

3. High isolation: The MEMS switch's exceptionally low OFF-state capacitance results in a good isolation profile up to 40 GHz.

4. High linearity. MEMS switches are exceedingly linear, that have 30–60 dB greater linearity than PIN diodes or FET switches.

Table 1.1 MEMS switches benefits and drawbacks

Advantages	**Disadvantages**
Low insertion loss	Low switching speed
High isolation	High actuation voltage [electrostatic switches]
Low power demand	Low power handling capabilities
Large bandwidth	Shorter Lifespan than relays
Miniaturization	Reliability uncertain
High signal linearity	High fabrication cost
High volume production	Complex integration with RF circuit

As a result, MEMS switches are intended to change the course of RF waves while maintaining signal purity. This function can be used to transfer an electrical potential, filter signals, such as the incoming and outgoing signals from an antenna, or reconfigure a subsystem, capacitors, switching delay lines in phase-shifters [4-6], as well as impedance matching via stub-lines [7]. Since the main RF subsystems in communication system applications include antennas, power amplifiers, and tunable filters [4], RF-MEMS switch is considered to be a foundational and essential component from a hardware perspective, especially in Fifth-generation (5G) applications nowadays. [4, 8-10]

In fact, a significant percentage of Internet of Things (IoT) data flow nowadays will be carried through 5G. This will manifest itself in demanding standards for RF passives in terms of frequency agility, low loss, high selectivity, and low consumption [8]. The forthcoming 5G standards' growing expectations create a recurrent demand for RF-MEMS passive devices. [10]. Furthermore, ohmic (DC contact) based RF-MEMS switches are used in automatic test equipment (ATE) and wideband electronics, such as in satellite systems for compactness and weight savings. In addition, MEMS ohmic contact switches show considerable potential in wideband transceivers, phased array systems, as well as, in microwave communication devices used in telecommunications networks [2].

1.2. Types of RF Switches

RF-MEMS switches are generally categorized according to their actuation mechanism; electrostatic [11], electromagnetic [12], piezoelectric [13], and thermal [14] techniques are often used. Due to its unusually high-power handling capabilities and compatibility with manufacturing procedures for high-level integrated circuits or systems [15], the electrostatically actuated MEMS switch presents a promising future for microwave applications.[15].

Besides, RF-MEMS switches are frequently designed in one of two ways: (fixed-free) cantilever or (fixed-fixed) bridge membrane. In comparison to a suspended membrane, the cantilever type offers a significant privilege such as a lower actuation voltage. However, cantilever switches are more prompt to residual mechanical stress in the material of the beam [16]. Usually, there are two types of RF-MEMS Switch configurations: shunt configurations (usually employs fixed-fixed based switches) and series configurations (usually utilize cantilever-based switches), which differ in terms of the position across a transmission line.

According to operating techniques, the RF-MEMS switch can also be characterized by its contact, whether it is an ohmic (DC) contact RF-MEMS switch or a capacitive contact RF-MEMS switch. The ohmic contact RF-MEMS switch operates at frequencies ranging from DC to 60 gigahertz as ohmic contact has small up-state capacitances. While the capacitive RF-MEMS switch has a frequency range up to 100 GHz since it is actuated by capacitance fluctuation. On the positive side, for frequencies less than 50 GHz, the ohmic contact RF-MEMS switch outperforms the capacitive RF-MEMS switch, in terms of structure simplicity, charging issues, stability, compatibility with a microstrip line, and durability [17]. Nevertheless, the major disadvantage of an ohmic switch over a capacitively coupled one is the deterioration of the contact metal, which results in a limited lifespan [18, 19].

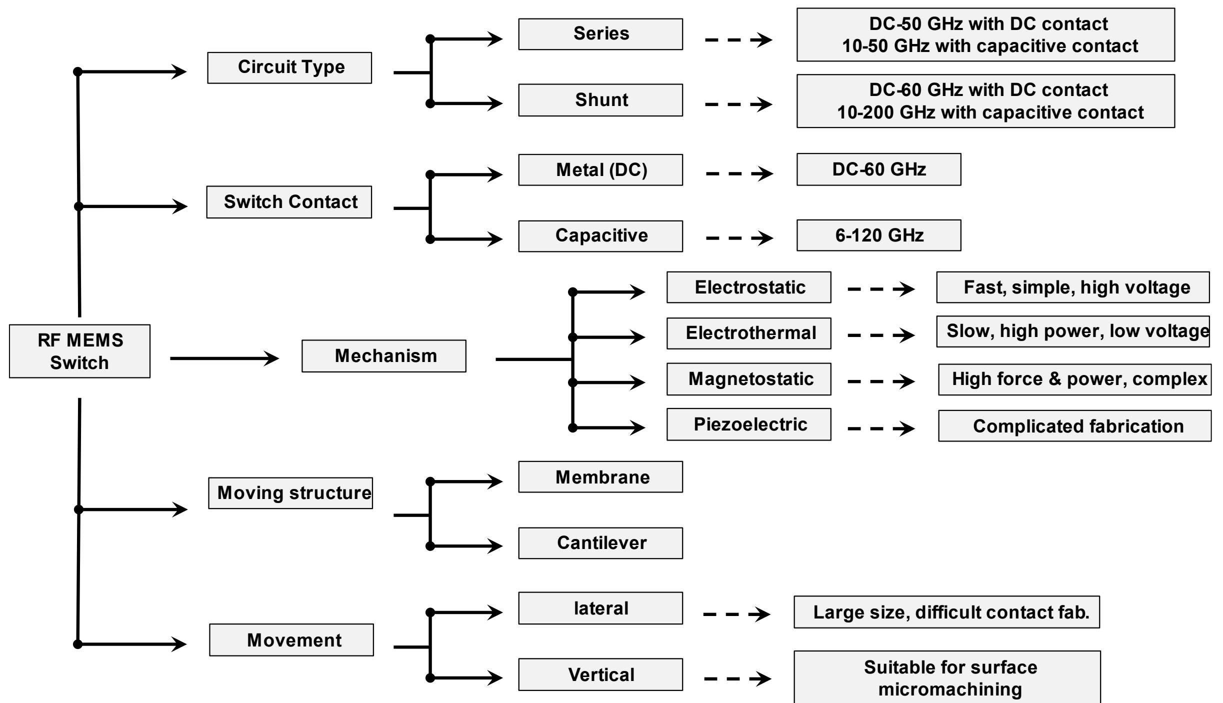

Figure 1.1 RF-MEMS switch Classification

Commonly, there are two most employed switch types, schematically illustrated in Fig. 1.1:

- **Series switches with DC metal contacts with electrostatic actuation (Fig. 1.2):** The signal line is opened or closed vertically using a cantilever or membrane with a metal contact (or ohmic DC contact); the suspended part will have direct contact to the signal line. In the OFF-state the switch is suspended in its original position, and the propagating RF wave is reflected by the broken signal line. While in the on-state, the signal can travel over the cantilever metal contact beam, shorting the air gap between the input and output lines. Even though, this switch type can switch DC to RF signals, it is more complex to fabricate and maintain due mostly to its metal -to- metal contacts.

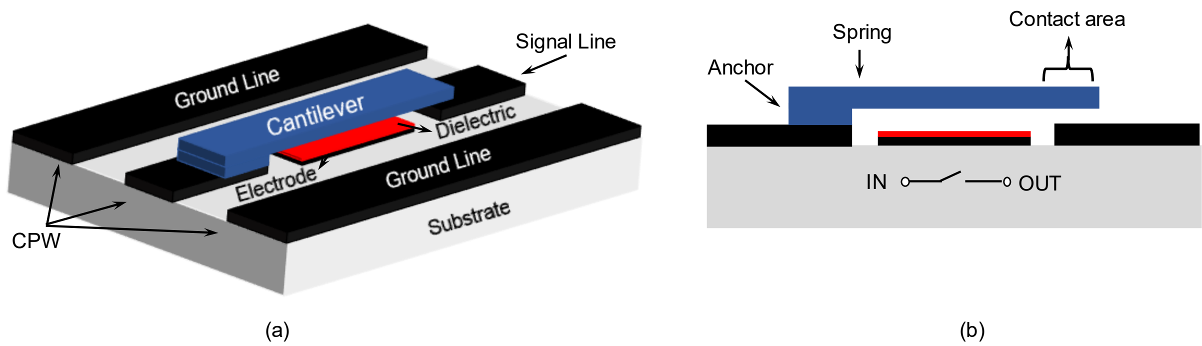

Figure 1.2 Cross section view for series switches with DC metal contacts with electrostatic actuation.

- **Capacitive shunt switches with electrostatic actuation (Fig. 1.3):** These structures are well suited for high-frequency (>10GHz) applications. Because it has a less parasitic impact when the switch is activated, the RF-MEMS capacitive switch is mostly used in a shunt-type configuration. In the on-state, the fixed-fixed membrane is suspended in its original position, with an air gap between the membrane and signal line; hence, the on-state capacitance is low, resulting in a high impedance between input and ground. While in the off-state, the fixed-fixed membrane is drawn down to the signal line, where there is only a very thin dielectric layer on the signal line, resulting in a large downstate capacitance and a low impedance between input and ground.

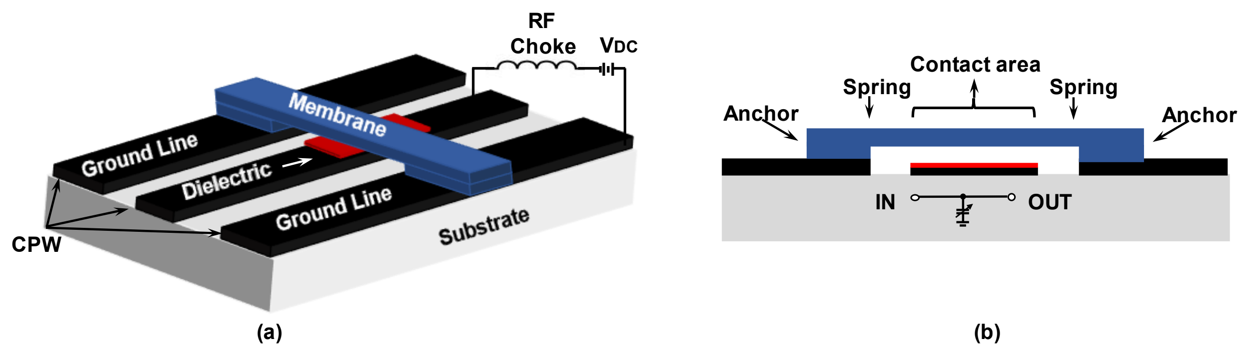

Figure 1.3 Cross section view for Capacitive shunt switches with electrostatic actuation.

1.3. Motivation

This research aims to explore the performance of cantilever-based RF-MEMS switch at high frequency to match 5G application demands. The motivation is to increase switching reliability and lower power consumption by lowering the voltage used to activate the

switch without compensating for the RF performance of the switch. To accomplish this goal, a list of objectives has been developed to guide the study:

- To design and simulate the behavior of a fixed-free micro-cantilever beam in a series arrangement using bidirectional control of intrinsic stress to generate self-assembled wavy switch structure that provide simultaneous optimization for actuation voltage and isolation..
- To design and optimize the behavior of cantilever-based shunt structure is proposed to realize a low-voltage RF-MEMS switch and high RF characteristics.
- To carefully model RF-MEMS switches using electromechanical and high-frequency finite element simulations in COMSOL and HFSS, respectively.
- To designs RF-MEMS switches with geometrical parameters that meet the fabrication criteria and are based on real fabrication step using standard CMOS technology.

1.4. Thesis Structure

The designs, analyses, fabrication processes, and measurements of high-performance RF-MEMS switches are the focus of this thesis. Fig. 1.5 depicts the structure of the analytical approach used in the construction of both RF-MEMS switches. It also describes the phases that had a significant impact on the switch's performance and provides a foundation for the development of RF-MEMS technology.

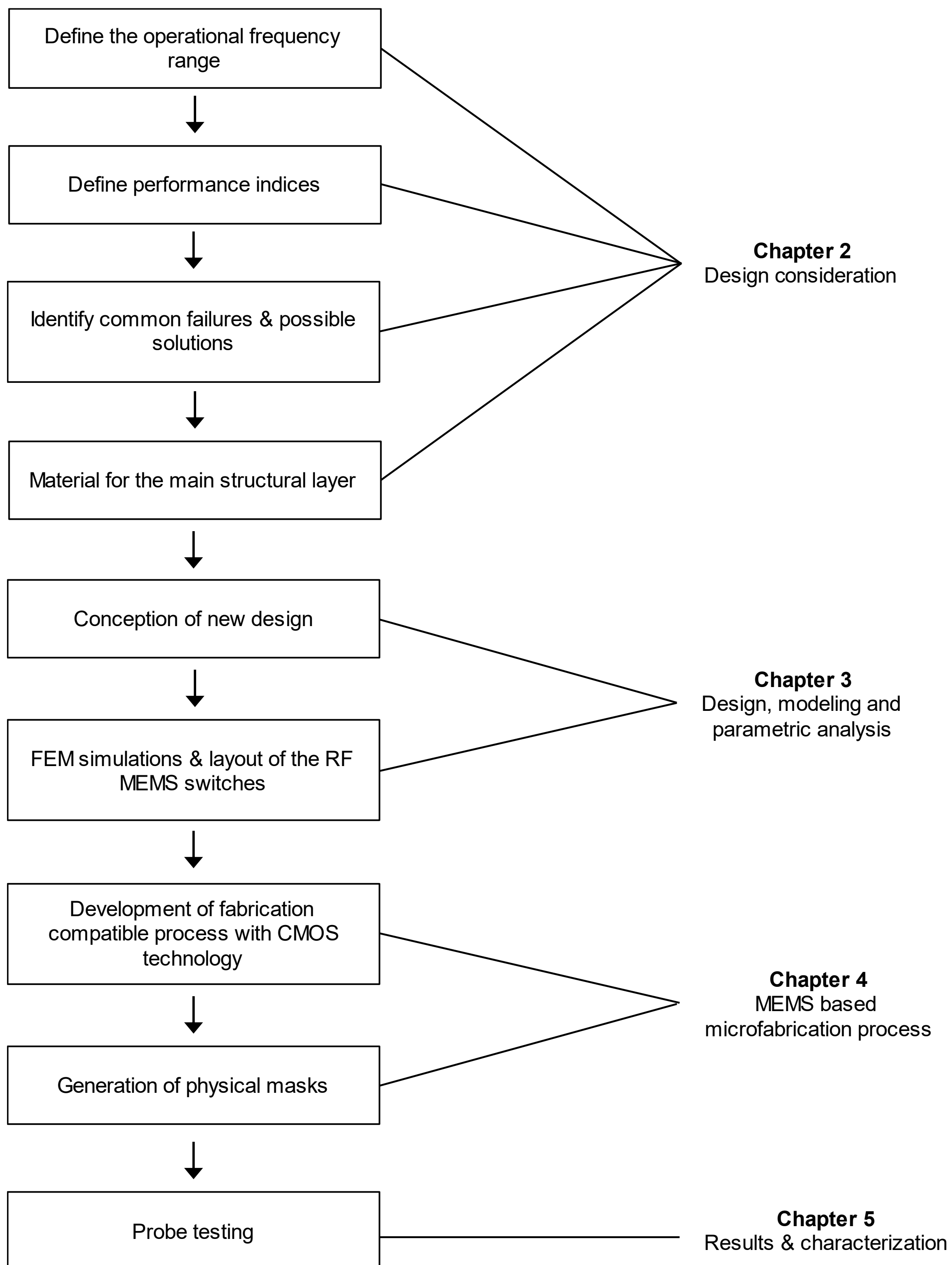

Figure 1.4 Analytical approach to developing the proposed RF-MEMS Switches.

The thesis is structured into 3 main chapters, which can be summarized as follows. Chapter 2 intention is not to recite the common knowledge in the field, but rather to focus on discussing, in a more extensive way, the switch design parameters considered and optimized in this thesis. Furthermore, the proposed cantilever-based RF-MEMS switches on two different configurations are explained conceptional in chapter 3, with further

design and modeling elaborations and design comparison to related existing work. While chapter 4 describes the basic fabrication process with its optimized parameters. Finally, chapter 5 discusses the fabrication measurements results, respectively.

II. DEVELOPMENT OF ELECTROSTATIC RF-MEMS SWITCHES

The majority of research literature describes novel switch designs and their characterization findings, as well as their general benefits and applications. Only a few publications address design-specific difficulties, explore the effect of a range of design characteristics, and contrast various perspectives [20-23]. This section discusses many challenges, and critical design issues associated with electrostatically driven cantilever-based RF-MEMS switches addressed within our designs. Also, it discusses the relationship between several design criteria and attempts to impart a sense of how to build a MEMS switch. Additionally, it addresses the primary dependability issues associated with contact switches. **Actuation Voltage, Displacement, And Restoring Forced**

Electrostatic actuation is based on the attraction of two plates with opposing charges. It is extensively used because it enables relatively simple fabrication [15]. The electromechanical instabilities, mainly the pull-in phenomena, are critical in providing quick actuation and low power consumption in RF-MEMS switches. However, this force is not directly proportional to the applied voltage [5]. Consider a system consisting of two plates (one suspended and one fixed) separated by a dielectric medium gap.

Electrostatic actuation generates relatively small forces, yet they are sufficient to actuate a MEMS switch. Once a direct current is placed between the fixed and moveable plates, the electrostatic forces are balanced by the suspended electrode's elastic restoring mechanical force. As the voltage increases, the movable plate is drawn down and the electrostatic force increases nonlinearly due to the decrease of the gap distance. The restorative force, on the other hand, works in the opposite direction.

Evidently, at a certain distance, the balance between the attractive electrostatic force and the restoring mechanical force becomes unstable, and the plate abruptly snaps onto the underlying fixed plate. This is referred to as pull-in, and the bias voltage level that causes the moveable membrane or cantilever to abruptly snap down is referred to as pull-in voltage or actuation voltage [3, 5].

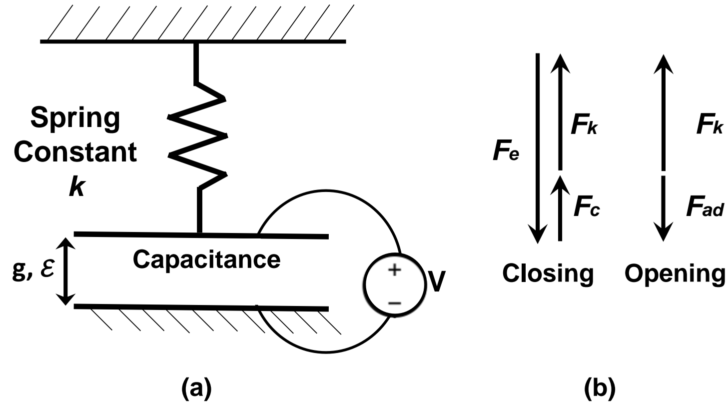

Figure 2.1 A simple spring-based switch representative (a) electromechanical equivalent circuit (b) active forces on the beam.

$$V_{pull-in} = \sqrt{\left(\frac{2}{3}\right)^3 \frac{g^3 K_{eff}}{\varepsilon_0 \varepsilon_r A_{eff}}} \tag{2.1}$$

where, ε_r is the permittivity of dielectric medium between the two plates, ε_0 is the relative permittivity of free space, A_{eff} is the effective overlapping electrode area, g is the air gap and k_{eff} is the effective spring constant. As can be seen, the actuation voltage is proportional to $g^{\frac{3}{2}}$ and indirectly proportional to $\sqrt{A_{eff}}$.

Overall, current electrostatic switch designs have pull-in voltages ranging from 40 to 100 V to provide adequate switching performance [24]. These voltages are incompatible with the voltage levels typical in electrical devices. Even though thermal and magnetostatic actuators may have pull-in voltages as low as 5 V, their significant power consumption is not tolerable in wireless applications [25].

In general, designing an efficient switch with small electrode actuation areas (for minimized chip size and low cost per switch), low pull-in voltages (for electronic suitability), , a sensible restoring force (for contact reliability), a high contact force (for low resistance), and a large contact distance (for high isolation) has proven to be difficult.

Table 2.1 A literature review summary

Technique	**Propose Designs**	**Freq. (GHz)**	**Voltage (V)**	**Isolation (dB)**	**Insertion loss (dB)**	**Return loss (dB)**	**Ref**

Lower spring constant (K)	Folded beams K= 0.22 N/m	20	2.2	-27.44	-0.2527	-11.35	[26]
	Serpentine Beams K= 1.43 N/m	38.6	$V_{pull-in}$=32.4 $V_{pull-out}$=11	-33	-0.056	-13.74	[27]
	reducing the beam thickness K= 1.43 N/m	40	$V_{pull-in}$=4.8 $V_{pull-out}$=2.8	-40	-0.4	-16	[28]
	push-pull Structures	10	$V_{pull-in}$=8.25 $V_{pull-out}$=9.5	-35	-0.38	-0.17	[29-31]
Large Actuation Area (A)	extend the actuation area A= 190x220 µm	3	0.5	-27	-0.1	-20	[32]
Small air gap (g)	Thin sacrificial layer g=1.5um	10	3.3	-40	-2	--	[33]
the residual stress	Curved electrode actuator	5	15.3	-44	-0.21	----	[34]
Graphene based switch	Monolayer	50	7	>-10	-0.3	-15	[35]
	Multilayer	50	7	>-20	-0.2	-15	

The RF-MEMS community is aware of this issue, as shown by the publication of several electrostatically actuated switch designs during the previous decade. For instance, some studies developed a switch with a lower spring constant, however, these designs experience a relatively low restoring force, which could be insufficient to pull the switch up, resulting in contact stiction. In order to overcome this problem, a pull-push mechanism is employed, which in turn increases fabrication complexity [26-28]. In another study [34], they utilize the residual stress gradient in beams to create an out-of-plane bending structure that lowers the pull-in voltage and increases the isolation -44dB @5GHz. Nonetheless, the stress level within a cantilever is difficult to control. While [31, 33], used a small air gap, at a cost of higher the insertion loss of around -2dB@ 10GHz. A literature review summary is shown in table 2.1.

2.2. Adhesion Between Actuation Electrodes

One of the most common failure sources of MEMS switches is undesired adhesion between the cantilever and the underlying electrode during operation, which results in contact stiction. This is originated due to the electrostatic stiction caused by the charge injection in trapping in dielectric layers, which is mostly reliant on the quality of the dielectric, the field strength (higher than 2 $MVcm^{-1}$) [36, 37], and the long period in the active state [38]. Consequently, the charging of the dielectric layer has received a lot of attention.

Besides the dielectric charging phenomena, silicon-based dielectrics (nitrides and oxides) are very hydrophilic and include absorbed water layers. Once two of these surfaces come into close contact, hydrogen bonds might form, resulting in a very high adhesion energy [39].

Therefore, the switch dielectric material as well as DC voltage supply setup help to minimize the failure from adhesion and contact stiction issues. In an effort to reduce the dielectric charging effect, silicon dioxide is preferred as a dielectric, since it has a lower trap density than silicon nitride and is, therefore, less susceptible to electrostatic stiction [40]. Another method to reduce the charge injection in the dielectric is by changing the DC voltage supply setup to an AC bipolar actuation voltage [41] or supplying the voltage exponentially and reducing the voltage [42].

2.3. Material

There are three main key metrics while selecting the appropriate material, for RF-MEMS switches; pull-down voltage, where the coefficient of stiffness k depends on Young's modulus, and Poisson's ratio of the material; RF losses, material conductivity; and thermal residual stress. In addition to the prior, the choice of structural material is influenced by the material resistance, hardness, and fabrication deposition complexity. Taking all into consideration, the basis of material selection diagrams [43] revealed that copper (Cu) and gold (Au) are the most suitable candidates as the main structural material.

The use of copper as the structural material has been studied in this work with the motivation of demonstrating that multiple MEMS devices can be fabricated simultaneously using existing high-volume IC copper-based interconnect manufacturing processes. From a performance standpoint, it is highly desirable to enable direct fabrication of all devices involved in the 5G communication system, including antennas, using current IC communication chips. In addition, the "direct integration" technique allows us to incorporate the MEMS device cost into the base cost of the IC connection layers [44]. Furthermore, copper is readily available and can be a low-cost alternative to gold (Au), along with added uses including the implementation of a floating metal layer with well-established routes from PCB process technology to control surface roughness and improve switch contact [45, 46].

It is also worth mentioning that Cu has a higher hardness that can minimize contact wear, as well as, relatively low resistivity required to reduce the losses at high RF frequency ranges. Finally, Cu has a relatively high thermal expansion coefficient, allowing it to work at higher temperature ranges. Therefore, reducing the chances of failure in the device due to self-heating at RF frequencies [47].

2.4. Residual Stress And Stress Gradient Tolerance

Residual stresses arise within microstructures throughout the microfabrication process and may be classified based on their origin; intrinsic or extrinsic stresses (thermal stresses, chemical reaction). Residual stress has a significant impact on material mechanical characteristics such as brittle fracture, creep cavitation cracking, shorter lifespan, stress corrosion, and dimensional stability [48].

When thin films are deposited on a substrate using common deposition processes (chemical or physical vapor deposition), they are susceptible to stresses known as intrinsic stresses. The nature (tensile or compressive) and amplitude of intrinsic stresses are exclusively determined by the material type, deposition process (evaporation, sputtering, etc.), and deposition circumstances (temperature, pressure, and so on) [49]. If the deposition conditions were maintained constant, there are strategies to control the degree of stress and keep the cantilever flat, such as utilizing stress compensation layers, and this can be addressed in fabrication process flow optimization [50].

2.5. Contact Area Verses RF Performance

Insertion loss is defined by the amount of energy that a signal loses as it travels along the signal transmission. When a signal is propagating, the ratio between the input and output terminals of the switched circuit is measured by $S21$, thus, the switch is said to be in the ON-state. The isolation of an electrical switching system is defined by the absence of the signal transmission and is measured by $S21$; thus, the switch is said to be in the OFF-state.

In the ohmic series configuration, the transmission line is shorted when voltage is applied, and the cantilever is pulled down to form a metal-to-metal contact with the transmission line. In this case, a RF-MEM switch will create resistance at the contact area between the cantilever beam and the transmission line, which is the main cause of Insertion loss, as it can be seen by the loss equation (neglecting transmission line loss) [5].

$$Loss = \frac{4R_s Z_0}{|Z_s + 2Z_0|} \tag{2.2}$$

However, in the ON-state, $Z_s = R_s + j\omega L$, and thus the loss becomes

$$Loss = \frac{R_s}{Z_0} \qquad for\ \omega L \ll Z_0 \tag{2.3}$$

$$R_s = R_c + 2R_{s1} + R_l \tag{2.4}$$

Typically, for ohmic cantilever switches, in series configuration, the total switch resistance (in equation 2.4) is composed of the contact resistance, R_c, between the contact regions that is proportional to its length and width, the transmission loss equivalent resistance, R_{s1}, and cantilever resistance R_l. The DC-contact switch is governed by R_c, which is created by the roughness of the contact surfaces. Undoubtedly, to achieve lower insertion loss in case of metal-to-metal contact, the contact resistance must be reduced. Henceforth, it is crucial to carefully consider the switch's material, the contact area, the force applied, and the quality of the metal-to-metal contact, to determine the contact resistance.

Unfortunately, calculating the contact resistance between two rough surfaces is challenging due to the presence of pores and bumps in the surface formed during

the contact fabrication. These have varied contact interference and may interact with one another [51]. Fig. 2.2 below illustrates the interconnected design parameters that contribute to the contact performance (the contact resistance and the contact reliability) of the switch.

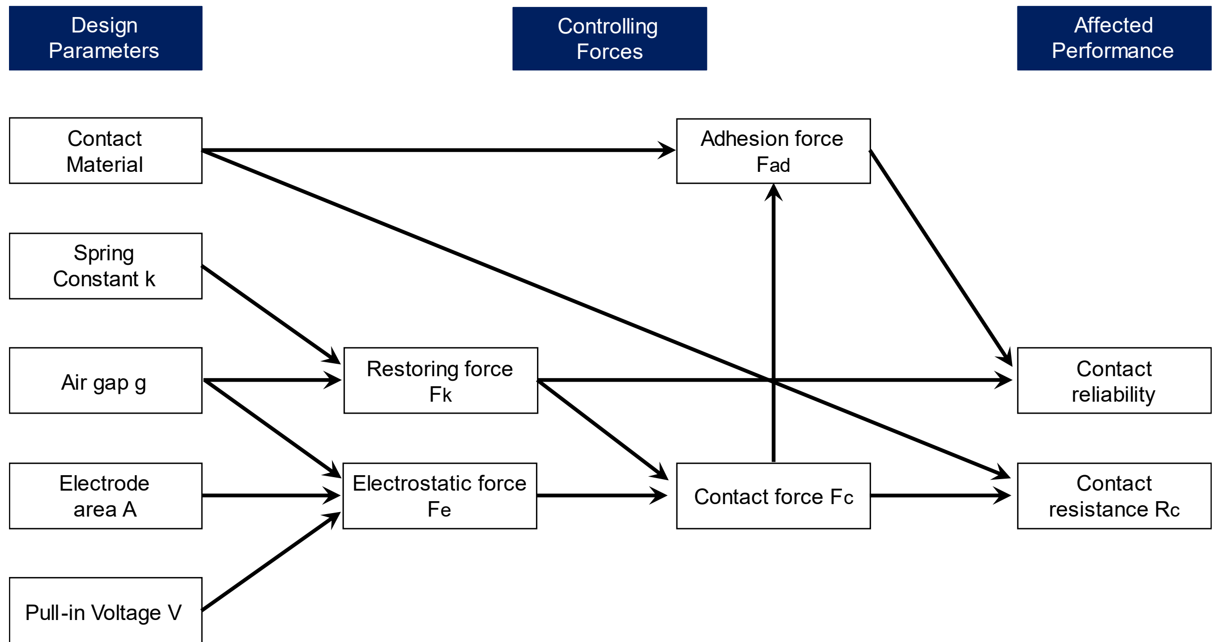

Figure 2.2 The interconnection between the design parameters that affect the contact performance.

To increase contact reliability and prevent contact stiction, a low contact resistance needs a strong contact force, as well as a high restoring force. A substantial restoring force may be achieved by combining a reasonably rigid structure with a large air gap, which enhances the electrostatic force drawing the structure downwards. Increasing the restoring force necessitates an increase in electrostatic force to maintain the correct contact force, demanding either a higher actuation voltage or a wider actuation electrode area. Therefore, it is complex to create a switch with a low actuation voltage for electronic compatibility, a small actuation electrode to reduce device cost and size, a large distance between the cantilever and RF signal line for high RF isolation, a high restoring force for contact reliability, and a high contact force for low contact resistance. Therefore, the optimization of switch behavior is a compromise between electromagnetics and electromechanical features, with the practicability of the technological process in mind.

On the other hand, in the case of capacitive shunt configuration, the transmission line is shorted when voltage is applied, and the cantilever, where the signal is channeled to

ground via the cantilever. In this case, the RF-MEM switch will result in capacitive contact with the transmission line due to the dielectric in between. The down-state capacitance should be large to achieve high isolation, thus from Eq. 2.5 contact area should increase.

$$C_{down/off} = \frac{\varepsilon_o \varepsilon_r A_{contact}}{t_d} \tag{2.5}$$

where ε_0 is the relative permittivity of free space, ε_r is the permittivity of dielectric material, and *g* is the air gap between the RF line and switch cantilever. Moreover, t_d is the dielectric thickness, and $A_{contact}$ is the contact area between the switch beam and RF line. $C_{down/off}$ is further explained in section 3.2.

2.6. Effect Of Up State Coupling Capacitance On RF Performance

The up-state coupling capacitance (Cup-state) is a key parameter in the RF-MEMS switch when it is in a resting state (up-state). In series configurations, the Cup-state is created when the switch is off, hence contributing to the isolation value. On the other hand, in shunt configuration, the Cup-state affects the insertion loss values.

Due to the current leakage between the suspended cantilever and the stationary transmission line, the s-parameters values degrade. The total up-state coupling capacitance is made up of series capacitance C_s, and C_p is the parasitic capacitance between the transmission line's open ends (seen in Eq 2.6) [3].

$$C_{up-state} = \frac{C_s}{2} + C_p \tag{2.6}$$

The series capacitance is further composed of a parallel-plate capacitance of the overlapping contacts area $C_{pp} = \frac{\varepsilon A}{g}$ and a fringing field capacitance C_F, which is around 30–60% of Cpp. Whereas parasitic capacitance between the transmission line's open ends is mostly determined by the distance between two signal lines.

2.7. Substrate And Transmission Line

Initially, substrate dimensions are optimized using substrate selection criteria. Thus, due to their low dielectric loss and high resistivity, quartz and borosilicate glass are often

utilized for RF device fabrication. These materials are less thermally conductive than silicon, harder to bulk micromachine, and not always suitable as a single platform for various MEMS [52]. Henceforth, highly resistive silicon (HR-Si), or silicon-on-insulator (SOI) substrates have been used instead. Since the charge collection at the interface between silicon and the silicon dioxide passivation layer, the effective resistivity of passivated HR-Si is several times lower than the bulk resistivity value [53]. Therefore, the switches are simulated on high-resistivity silicon substrates, with a thick layer of silicon dioxide used as a buffer layer in order to improve such losses in HR-Si. [54]. The switches were also simulated and fabrication on Borofloat33 glass in hopes of integrating the entire 5G circuitry elements (antenna, dividers … etc) on the same mask, because glass substrate has a dielectric constant of 4.6 suitable for antenna functionality.

Followed by substrate selection, the transmission line is determined from the application aspect as well as the material skin depth effect [3, 55]. Several transmission line topologies (e.g., slot line, coplanar waveguide (CPW), and microstrip line) were investigated for designing the proposed RF-MEMS switches. Among these configurations, the CPW transmission line was chosen for its effectiveness in controlling the RF line's characteristic impedance and its simplicity of integration with mm-wave circuitry. Additionally, CPW incorporates ground planes on both sides of the signal line, which reduces dispersion and radiation leakage, hence lowering the switch's overall insertion losses [55].

III. DESIGN AND MODELING OF CANTILEVER TYPE RF-MEMS SWITCHES

The multidisciplinary character of MEMS switches necessitates a very close coupling between the electrical and mechanical domains. To aid in the understanding and characterization of RF-MEMS switches, the finite element modeling (FEM) approaches are employed in MEMS electromechanical simulation software. The finite element

modeling method can predict how a load will affect a body's mechanical and nonmechanical responses, such as force, moment, temperature, electromagnetic field, and any other load affecting the body. The simulation component is separated into distinct pieces that interact at the nodes. Certainly, FEM simulates more realistically and accurate than system-level modeling, but it takes more computing power. In this thesis, the electromechanical and electromagnetics evaluation of RF-MEMS switches were performed using COMSOL and ANSYS Multiphysics simulation (HFSS, Canonsburg, PA), respectively [56-58].

In our work cantilever-based switches are designed in 2 different configurations (series and shunt) suitable for 5g application. The designs address the challenges facing each topology and take advantage of their benefits (see table 3.1). Moreover, according to section 2.3, Cu has been used as the switch material in this thesis.

Table 3.1 Advantages of series and shunt topologies

Type	**Default state**	**Advantage**	**Disadvantage**
Series	OFF-state	High isolation Low pull-in voltage Larger contact distance	Beam Buckling Contact force dependency
Shunt	ON-state	Low insertion loss Independent from contact force	Larger pull-in voltage

Initially, the chapter investigated the concept of intrinsic stress modulation throughout the length of a cantilever in its typical series configuration, in section 3.1. Followed by integrations and optimization of a cantilever switch realized in shunt configuration, which is more non-conventional, in section 3.2.

3.1. Wavy Cantilever RF-MEMS Switch Design

3.1.1. The Switch Concepts

The typical and most prevalent concept of an electrostatically actuated switch, as mentioned in section 2.1, is built on a cantilever-spring mechanism. This approach raises a few trade-offs between different switch design parameters. These trade-offs associated

with series cantilever-based switch configurations are represented in table 3.2. For example, a large air gap distance between the transmission line and the suspended cantilever is required for high off-state isolation and high restoring force. However, a large air gap results in a higher actuation voltage, which is not desirable.

Table 3.2 RF-MEMS switch in a series configuration

Design Parameters	**Isolation (UP-State)**	**Insertion Loss (Down-State)**	**Pull-in Voltage**	**Restoring Force**
Larger Air Gap	Higher (Good)		Higher (Bad)	Higher (Good)
Larger Electrode Area		Higher (Bad)	Lower	
Lower Spring Constant			Lower	Lower
Larger Contact area	Higher (Bad)	Lower		

As shown in figure 3.1, stress imbalance in a multilayer thin film can be taken advantage of to induce an out-of-plane twisting in formed thin films following release. In the meanwhile, the degree of stress-induced bending may be further regulated by altering the layer thicknesses while keeping the deposition parameters unchanged. Thus, permitting a controlled self-assembly procedure to transform patterned thin films into desirable out-of-plane 3D microstructures [49].

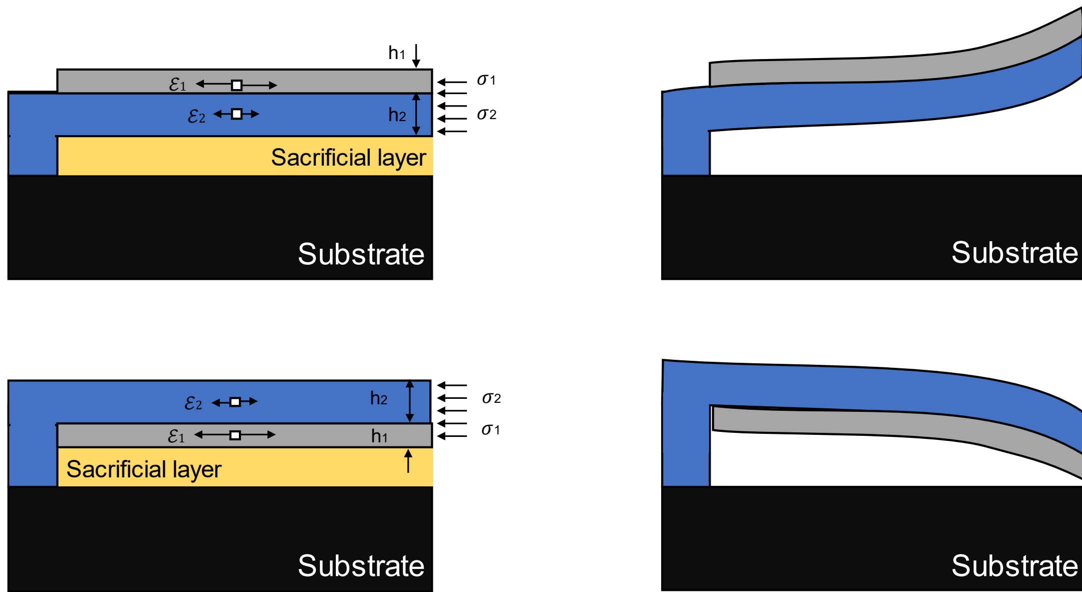

Figure 3.1 Schematic diagram showing the induced bending in bilayer thin film system when subjected to residual tensile stresses. The stresses σ1 and σ2 are the misfit stresses in the Cr and Cu.

Likewise, a recent work reports a quantified study on the geometrical effect on the amount of bending of thin-film cantilever structures [59]. Primarily, the study is carried out on series of bi-layer cantilever structures using copper (Cu) and chromium (Cr) as stacked metal layers to induce the bending angle relative to the geometrical requirements of the cantilevers. Typically, thin Cr film develops high intrinsic stress, which allows it to serve as the major stressor layer in the bi-metallic cantilever construction. From the study analysis shown in Fig. 3.2, it can be seen that the bending angles are proportional to cantilever length. However, the bending angle decreases with the increase in cantilever thickness for 300 nm, 500 nm, and 700 nm thicknesses. Therefore, by alternating stress conditions, the stress gradient sign can be controlled by increasing the tensile stress to develop positive stress gradients away from the sacrificial layer-thin film interface and negative stress gradients towards the sacrificial layer interface.

The presented switch design in this thesis is based on the theory of intrinsic stress induced bending in bi-metallic thin-film cantilevers. The standard beam cantilever design is improved by adapting an upward bending actuator that moves in a zipper-like manner.

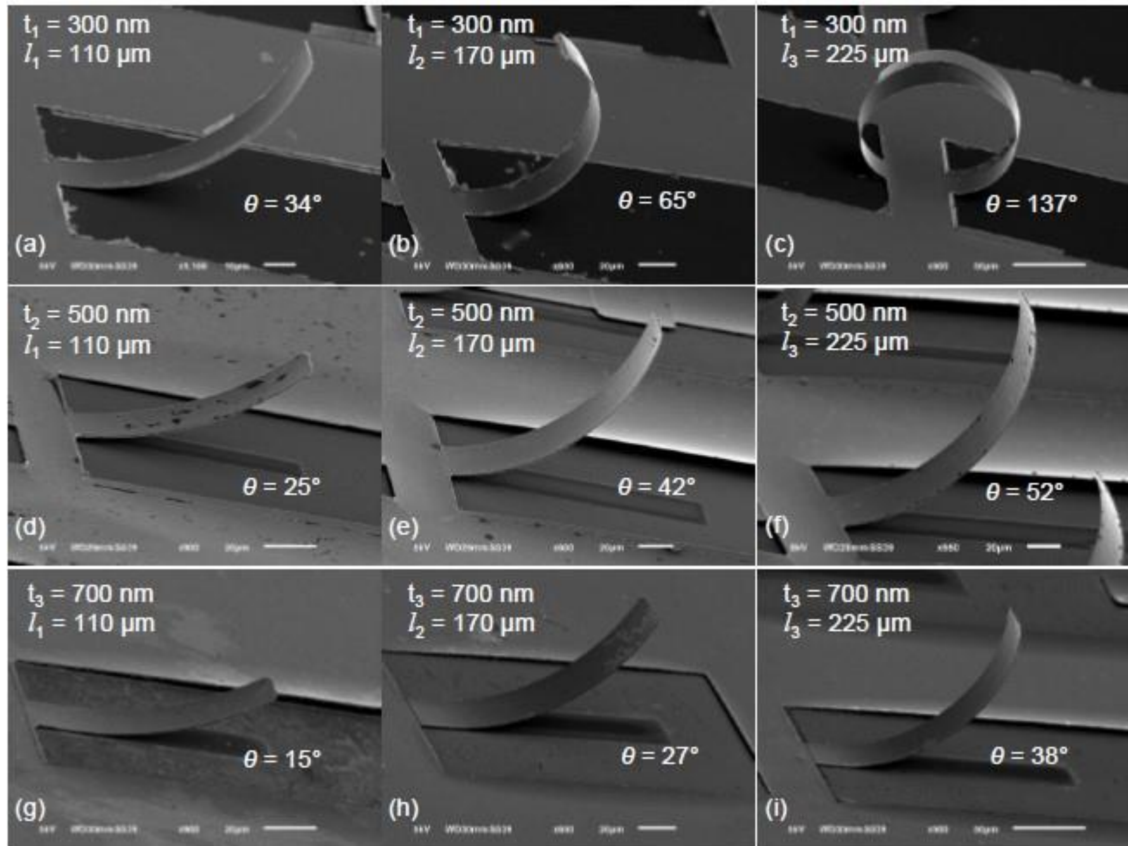

Figure 1.2 Bending profile for varying cantilever lengths and fabricated at three different film thicknesses [57].

Several curved electrode zipping actuators have been reported, owing to the upward bending in the cantilever type switches, the contact distance between the switch cantilever and the signal line increases which in turn increases the isolation of the switch in the up-state position (OFF-state). However, due to the bent profile of the cantilever, more voltage beyond the effective pull-in voltage level (necessary for the air gap) is typically required to provide adequate contact between the distal end of the cantilever switch and the signal line underneath [60]. To balance this trade-off, a stress control approach was used throughout the length of the cantilever, resulting in the switch structure seen in Figure 3.3.

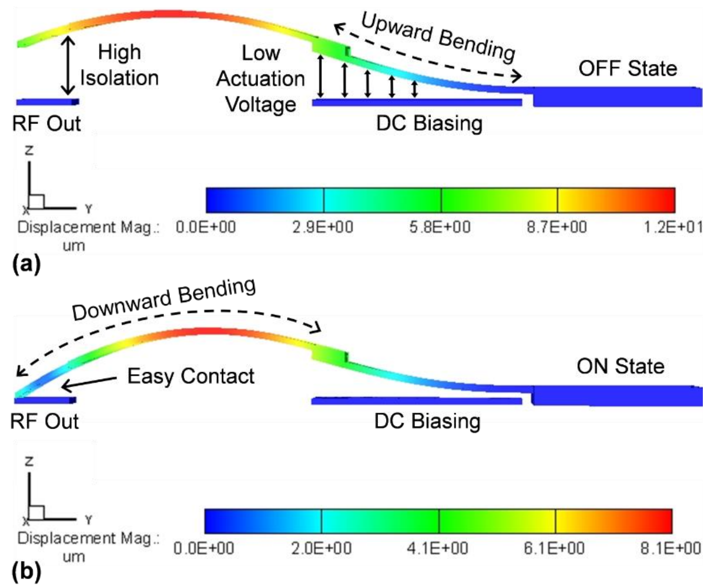

Figure 3.3 Wavy Cantilever RF-MEMS Switch based on Bidirectional Control of Intrinsic Stress [61].

The proposed cantilever switch featured 2 parts with different stress conditions, with the first segment (near the cantilever's anchor) exhibiting upward bending and the second segment (near the cantilever's free end) displaying downward bending. The upward bending in the cantilever raises the whole structure and immediately enhances the switch's isolation performance, whereas the downward bending at the free end of a cantilever ensures proper contact with the transmission line at pull-in voltage.

3.1.2. Switch Design

Several switch designs (with varying geometrical characteristics) were initially modeled, with the goal of achieving low insertion loss, maximum RF isolation, and reduced actuation voltage. The cantilever beam was released on CPW structure on (30/100/30) glass substrate and (60/100/60) HR-silicon.

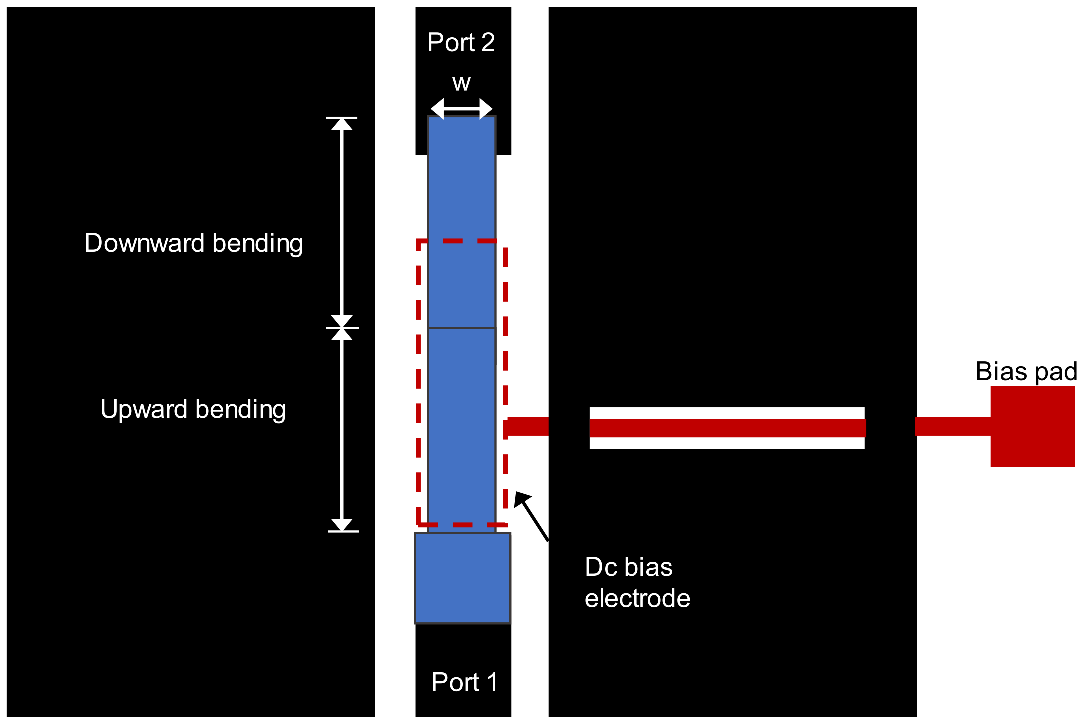

Figure 3.4 Top view of the proposed Series RF-MEMS switch.

A 2D top view of the suggested cantilever type wavy RF-MEMS switch is shown in fig. 3.4. To regulate the bending of metallic multi-layer stacks, the stress gradients along the thickness of the stack can be varied by adjusting the Cr and Cu thicknesses. Keeping in mind, Cu/Cr cantilevers with reverse stress gradients should bend upward, whereas Cr/Cu cantilevers with forward stress gradients should bend downwards, resulting in a switch with a wavy bending profile. Following that, a parametric design space was established with length (L) ranging from 300µm to 600µm and width (w) ranging from 50µm to 80µm to analyze the influence of geometrical factors on key RF parameters and bending outline (which primarily define the pull-in voltage and isolation).

Regarding zipping actuators' actuation, a pull-in electrode is necessarily placed near the fixed end of the bending beam (see fig. 3.4). The minimal gap between the electrode and cantilever affects the pull-in voltage. Zipping actuators operate well only if the two are near the edge of the anchor. Therefore, the DC bias electrode (with dimensions of (w) x ($\frac{3}{4}L$)) was placed near the cantilever's anchor point, where the air gap between the switch cantilever and the underlying DC electrode is minimal, promising lower voltage actuation. While the bias lines to the pull-down electrode runs underneath the CPW and are routed from outside of the CPW ground. In addition, there is a thin 0.2µm silicon

nitride dielectric layer on top of the electrode to isolate the electrode and avoid the direct electrical contact between the metal electrodes.

3.1.3. Electrical and Mechanical Simulation of the RF Switch

From there, the designed switch layout was examined in an interconnected simulation environment. The intrinsic stress, pull-in voltage analyses, and high frequency studies were all carried out using commercial finite element tools (COMSOL and ANSYS HFSS®). The following are the results from the proposed switch on a glass substrate as well as high resistive silicon (appendix A):

3.1.3.1. Electromechanical Analysis

Conveniently, as mentioned in section 3.1.1 the true magnitude of intrinsic stress in thin films is heavily reliant on the film thickness and deposition conditions. It is possible to modify the stress gradients along the thickness of a metallic multilayer stack by fixing the deposition parameters and ranging the Cr and Cu thicknesses. Firstly, a 2-D model implementation of the switch geometries was initially built in COMSOL using the designed parameters in fig. 3.4. The Cu/Cr metals were chosen as the simulator material, and their intrinsic stress mismatch is approximately 1.2 GPa. Accordingly, the stress values were given to the interfaces of structural layers.

The electromechanical simulations shown in fig. 3.5 of the switch under bidirectional stress demonstrate a wavy shape with combined total beam thicknesses of 830 μm (upward bending) and 870μm (downward bending) that results in a considerable gap of 40 μm between the RF line and the switch beam.

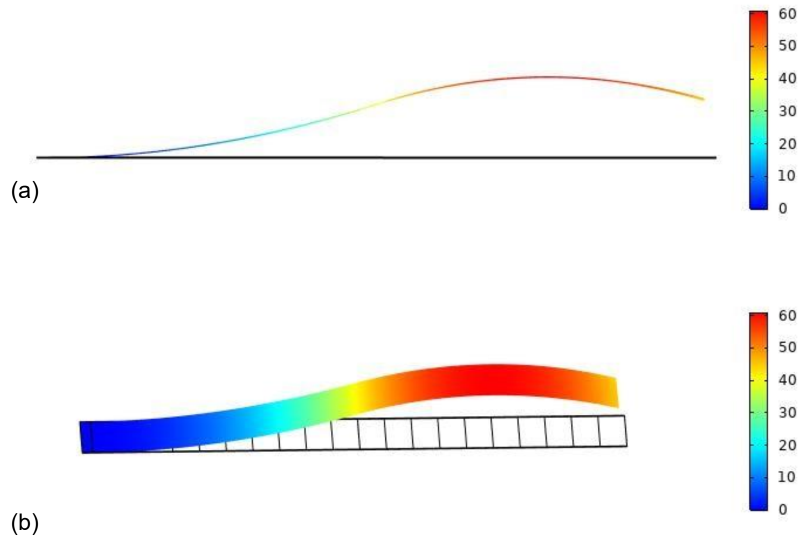

Figure 3.5 Bending profile of wavy switch cantilever.

The actuator tip deflections were simulated across various biasing voltages from 0 V to 50 V in a step of 0.2 V. Fig. 3.6 shows the plot of displacement as a function of biasing voltage for a zipping actuator with a length of 500 µm and a width of 100 µm. At the pull-down voltage, the solution becomes unstable, and the simulator is unable to calculate any further convergence between electrostatic and mechanical energy. The cantilever's tip steadily descends until it reaches a maximum deflection of 8.8 µm before collapsing into the bottom electrode at 40.5 V. As a result, the cantilever tip deflection is 22% of the original.

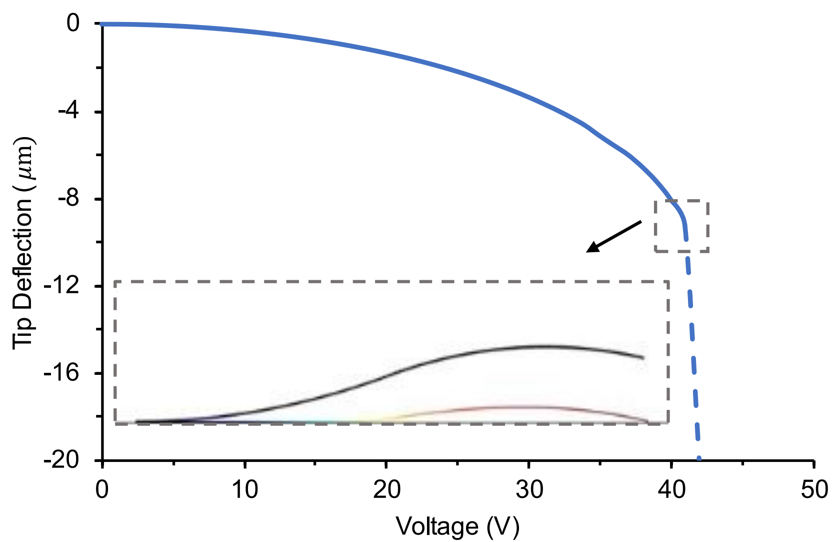

Figure 3.6 Tip displacement vs applied DC actuation voltage.

3.1.3.2. Electromagnetics Analysis

Similarly, electromechanical simulation deformed geometries were uploaded to ANSYS HFSS for high frequency analysis. In order to extract the S-parameters for switch geometries, a frequency sweep was performed using two-port analysis. In fig. 3.7, the switch's up-state isolation (S21, OFF-state) and down-state insertion loss values (S21, ON-state) were obtained and plotted against the switch's geometrical parameters. As previously stated, the contact resistance mainly defines the insertion loss, which is also dependent on the contact area. This can be seen from the plot. Insertion loss values vary from -0.4 dB to -0.8 dB for a given design space of lengths and widths, with shorter values of length and broader width implying a low contact resistance path and hence low insertion loss. Aside from the contact resistance, the change in width of the cantilever alters the switch impedance from the t-line impedance. The insertion loss was found to be -0.44 dB (@30 GHz) for 300 μm length with 100 μm breadth, as the line impedance remains unchanged and matching.

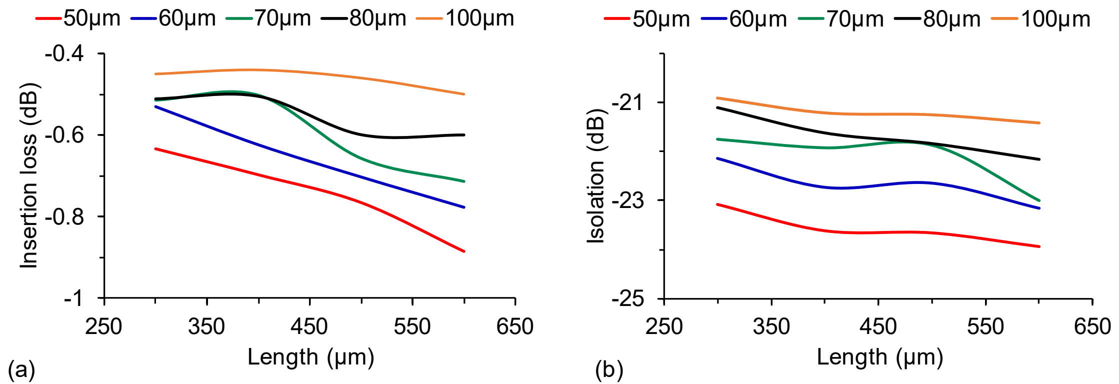

Figure 3.7 Performance against the switch's geometrical parameters (a) Down switch position (ON-state), (b) up switch position (OFF-state).

Likewise, Fig. 3.7b shows RF isolation for various switch dimensions. Due to the fact that a wider switch cantilever ensures a larger contact area between the switch cantilever and the RF transmission line, the coupling off-state capacitance increases, resulting in worsening the off-state RF isolation. Additionally, while maintaining constant stress conditions, the value of isolation improves with length, as increased length results in increased tip displacement (contact distance) which in turn reduces the coupling off-state capacitance. However, the contact distance is kept constant 40 μm for consistency in Fig. 3.7 simulations. To conclude, for switch dimensions of 50 μm (width) x 600 μm (length),

the maximum isolation value was determined to be -24 dB (@ 30 GHz). Therefore, in order to reduce the switch inherited trade-off, we designed a 100 µm cantilever switch width with a reduced contact tip width of 50 µm. The S-parameters of the optimized RF-MEMS switch on glass substrate are shown in Fig. 3.1, while simulations on high-resistive silicon are represented in Appendix A1.

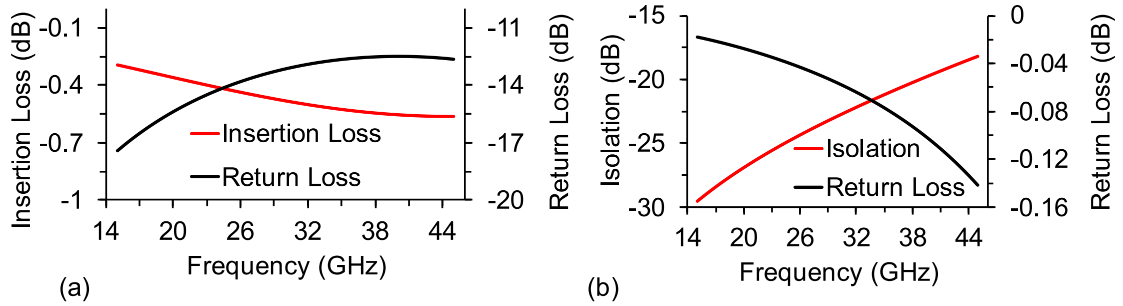

Figure 3.8 Simulated S-parameters of wavy RF-MEMS switch in the (a) ON-state and (b) OFF-state position with Vpull-in = 40 V.

Table 3 compares the performance of the suggested switches to that of relevant literature to provide clarification for the study's conclusions. To conclude, the obtained RF and mechanical performance data strongly support the proposed wavy cantilever RF-MEMS switch's efficacy in millimeter wave (5G) frequency ranges up to 50 GHz.

Table 3.3 Performance comparison of different simulation literature

Ref.	**Frequency**	**Isolation**	**Insertion loss**	**Pullin voltage**
[62]	Up to 110GHz	> -15GHz	< -1dB	50V
[63]	5GHz	- 44dB	-0.21dB	15.3V
[64]	Up to 10GHz	> -20dB	< -0.2dB	46V
[65]	Up to 40GHz	-36dB	-0.43dB	60V
Our Work	Up to 50GHz	> -20dB	< -0.6dB	40.5V

3.2. Cantilever Based Capacitive RF-MEMS Shunt Switch Design

3.2.1. The Switch Concepts

Generally, for high frequency applications, RF-MEMS switches employ capacitive shunt topology, because of their lower RF parasitic and insertion losses [66]. To realize a shunt configuration in RF-MEMS switches, a bridge membrane is often utilized that is suspended over the RF line and shorts the RF signal to ground when actuated [67]. Usually, shunt configurations are often used for high-frequency (>10 GHz) applications, and subsystems such as transmitters to shunt the signal to the ground and also used in receivers as shunt RF-MEMS switches are high reliability for low-RF power. [5]. However, since bridge membranes inherently possess large spring constants, their actuation commonly requires strong electrostatic forces, thus resulting in high pull-in voltages and slower switching speeds. While minimizing the pull-in voltage, a crucial trade-off typically originates between the pull-in voltage and corresponding RF performance parameters of the switch (i.e. isolation and insertion losses) [5]. For instance, an increased membrane size for switch results in a lower actuation voltage, but simultaneously increases the high-frequency ON-state insertion losses. Thus, simultaneous optimization of actuation voltage and RF characteristics of MEMS switches is essential to validate their applicability for mm-wave circuits [67].

Consequently, in this design, we investigate a cantilever-based shunt structure to optimize the switch S-parameters and lower the pull-in voltage RF-MEMS switch. In contrast, to shunt switches using a bridge membrane, we use a low spring constant fixed-free cantilever beam in a shunt configuration to reduce the pull-in voltage, which also offers faster switching speed and simpler design [16], while enhancing the RF performance by leveraging the inherent advantages of shunt topology. The proposed switch displayed in Fig. 3.9 is simulated on glass substrate, using CPW transmission line configuration to limit the RF losses.

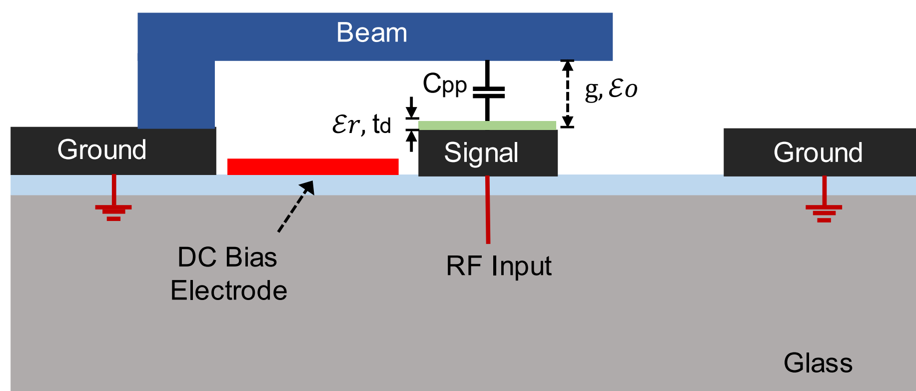

Figure 3.9 Cross-sectional view for the proposed cantilever-based RF-MEMS shunt switch.

When no actuation voltage is given, the electrostatic cantilever-based shunt switch remains in the "up" position, creating a small capacitive coupling between the cantilever and the RF signal line. Due to the large impedance associated with the up-state capacitance, the RF signal is routed thru the RF signal line, avoiding the capacitive path from the switch to ground. Likewise, the up-state capacitance $C_{up\text{-}state}$ between the switch and RF line in the up-state (on-state) is given as:

$$C_{up-state} = \frac{\varepsilon_o A_{contact}}{g + t_d/\varepsilon_r} \quad (3.1)$$

Conversely, when an actuation voltage is applied, the electrostatic forces pull the switch cantilever downward towards the RF line. As a result, the capacitance increases abruptly, thereby decreasing the corresponding impedance between the RF line and switch beam significantly. Consequently, when fully actuated, the switch beam establishes a capacitive contact with the RF line, thus providing a low impedance path between the RF line and the ground plane. Accordingly, the down-state of the switch refers to an OFF-state, where the RF signal is grounded via the switch beam. Once actuated, the gap (g) between the switch beam and RF line becomes zero, and hence, the down-state capacitance is shown in Eq. 2.5.

Furthermore, the ratio of down-state and up-state capacitances can be utilized as an indicator to evaluate the performance of the RF switch [66]. For instance, a small up-state capacitance corresponds to a low capacitive leakage in the up-state of the switch, thereby indicating low insertion losses and vice versa for the down-state. Therefore, the prime focus of our switch design is to maximize the capacitance ratio (r), which can be mathematically expressed as [68]:

$$r = \frac{C_{down-state}}{C_{up-state}} = \frac{(\varepsilon_r g + \mathrm{td})}{t_d} \cdot \frac{A_{contact}}{A_{contact}} = \frac{\varepsilon_r g}{t_d} + 1 \quad (3.2)$$

3.2.2. Switch Design

The proposed switch, illustrated in Fig. 3.9, was released on a Cu CPW transmission line deposited on a glass substrate. The transmission line impedance changes as we load the

line with the RF-MEMS switch due to the additional coupling capacitance created by the suspended beam above the transmission line. This results in a mismatch between the switch impedance and port impedance. When the switch is ON (in UP-state) a high coupling capacitance is created, resulting in a high return loss. In order to reduce the up-state return loss, we need to compensate for the high coupling capacitance by using a high impedance line at the desired frequency band [69, 70]. In this case, the CPW was modeled with a width of 100 μm for the central line conductor and a gap of 250 μm between the ground and signal line, to give an impedance value of 74.8 Ω. Whereas the thickness of the CPW transmission line was calculated based on skin depth to allow for the transmission of surface currents [71]. Cu was also employed as a conductive material for the switch, it has a skin depth of 0.381 μm at 30 GHz. As a result, the thickness of CPW was fixed to 1 μm to ensure efficient transmission of surface currents and electromagnetic radiations [72].

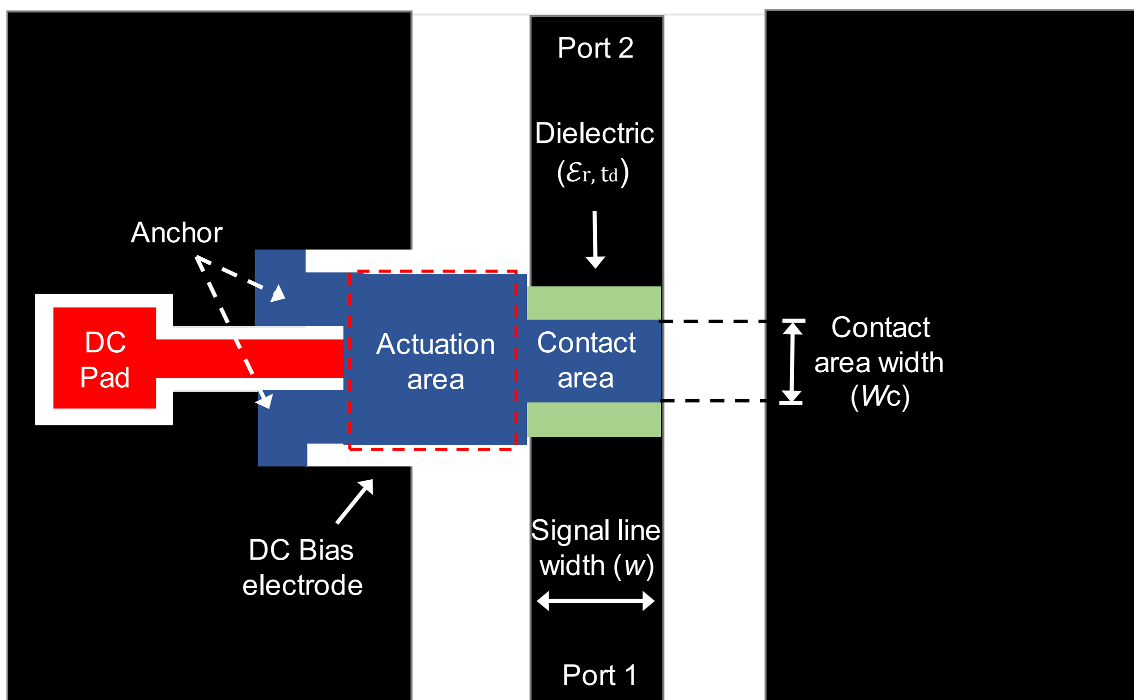

Figure 3.10 The proposed cantilever-based shunt RF-MEMS switch

Correspondingly, the actuation area is fixed to 200×100 μm^2 while the contact area width "Wc" is varied from 50×100 μm^2 to 200×100 μm^2, to search for an optimal RF response of the switch with respect to the up-state capacitance and down state contact resistance. A summary of the mechanical components of the switch with their dimensions is given in table 3.4.

Table 3.4 Structural Elements and Geometry of the Switch

Structural Elements	Material	Dimensions, x-y-z (μm)
Passivation layer	SiO_2	1900 x 2000 x 1
Coplanar Waveguide	Copper	1900 x 100 x 1
Biasing pads	Polysilicon	75 x 75 x 0.2
Actuation electrode	Polysilicon	200 x 150 x 1
Switch contact tip	Copper	50-200 x 100 x 1

3.2.3. Electrical and Mechanical Simulation of the RF Switch

The switch is meticulously modeled using electromechanical and high-frequency finite element simulations in COMSOL and HFSS, respectively. Furthermore, the suggested switch design is optimized for electromechanical responsiveness, lowering the actuation voltage even further and ensuring reliable operation. Finally, a parametric analysis is performed to determine the link between the geometric characteristics of the proposed switch design and its RF performance.

3.2.3.1. Electromechanical Analysis

To explore the impact of cantilever geometry on the electromechanical response of an RF-MEMS switch, we evaluated 3 separate cantilever switch designs, as schematically represented in Fig. 3.11. To begin, a simple cantilever was developed, denoted by "Case-1" (fig. 3.11a), followed by a non-uniform beam was examined in order to minimize the effective spring constant, as illustrated in Fig. 3.11b, refer to as "Case 2." Apart from optimizing the pull-in voltage, the durability of RF-MEMS switches is crucial for real-time applications in which these switches are required to fulfill billions of cycles [66]. One major drawback of electrostatic MEMS switches is the dominance of adhesion forces at an interface between the actuation electrode and switch beam, which causes beam stiction, thus damaging the device permanently [73, 74]. Therefore, a perforated non-uniform switch beam was considered as a “Case-3” in this work (Fig. 3.11c), to create

etch holes for both easily releasing the structure during sacrificial layer etching, and minimizing stiction issues [75].

Similarly, in line with the RF line's structural requirements, copper was chosen as the cantilever material, with a thickness of 1 µm. Additionally, a thin silicon dioxide layer (200 nm) was deposited to act as a buffer layer as well as isolate the fixed actuation electrode from the switch cantilever electrically. The air gap (g) between the actuation electrode and the cantilever was set to 4µm. The material attributes were adapted from the basic material library already included in COMSOL. Due to the symmetry of the geometry of all three beams, only half of the system was modeled using COMSOL's solid mechanics module, which decreases the computational burden. In order to determine the pull-in voltage and related tip deflection of the switch cantilever, a static study was performed.

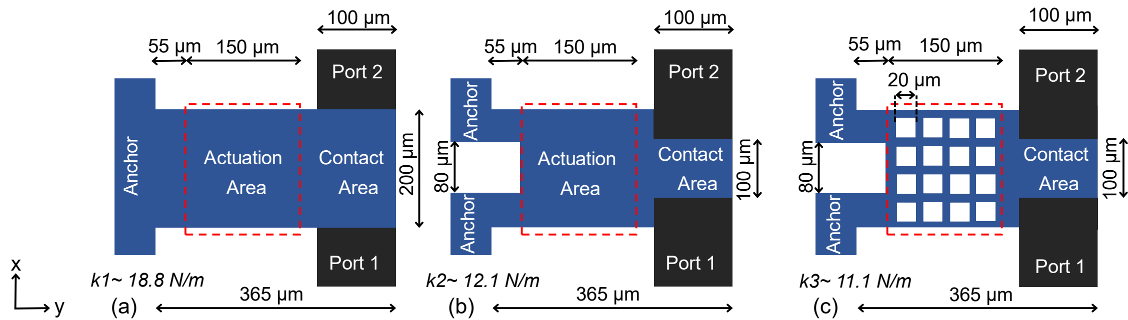

Figure 3.11 Schematic view of the RF switches: (a) Case 1, a simple cantilever; (b) Case 2, a non-uniform cantilever; (c) Case 3, a non-uniform cantilever with square perforations.

The variation in normalized tip deflection (δ) of switch beams with respect to the applied voltage reveals pull-in voltages for Cases 1 to 3 as 10.8 V, 9.1 V, and 9.8 V, respectively, where the system becomes unstable thereby indicating a beam-electrode contact. Case 1 exhibits the highest pull-in voltage among all other cases, which can be attributed to its high spring constant, as it is deemed to have a stronger and uniform anchor boundary condition and a higher moment of inertia. While the pull-in voltage for Case 3 is larger than that of Case 2, since the overlapping area for Case 3 is lower, which directly increases the pull-in voltage, as indicated by Equation (2.1). Conclusively, Case 2 performs the best in terms of pull-in voltage, while Case 3 provides a more reliable solution in terms of reducing potential stiction events with minimal sacrifice of less than 1V from the pull-in voltage. The electrostatic energy at pull-in voltages was also

estimated and found to be in the range of 1.5—2.5 pJ. Regarding supply voltages, CMOS typically offers below 1V supply, therefore solutions such as charge pumps will be needed to boost the voltage to the required pull-in values [76].

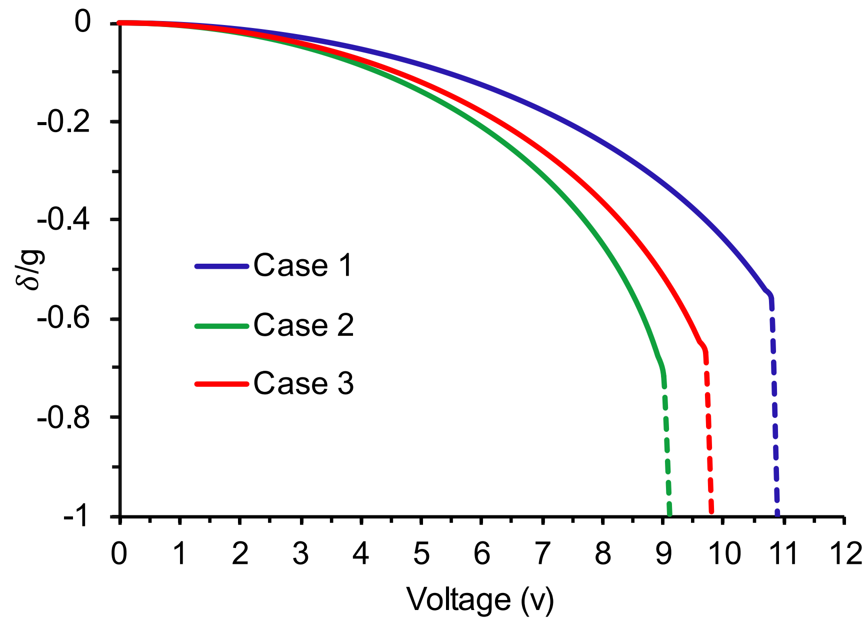

Figure 3.12 Normalized tip deflection vs applied DC actuation voltage.

Furthermore, the dynamic behavior of the switch cantilever at pull-in voltage was explored using a time-dependent study in which the motion of the cantilever tip from its initial free state to its contact state was observed (see fig. 3.13). The analogous outcomes from a time-dependent analysis are shown in Fig. 3.12, under which "Case 2" and "Case 3" exhibit comparable time-dependent performance at the pull-in state, with a switching time of approximately 90 μs. But the switching time for the simple uniform cantilever switch in "Case 1" is slower, around 120 μs.

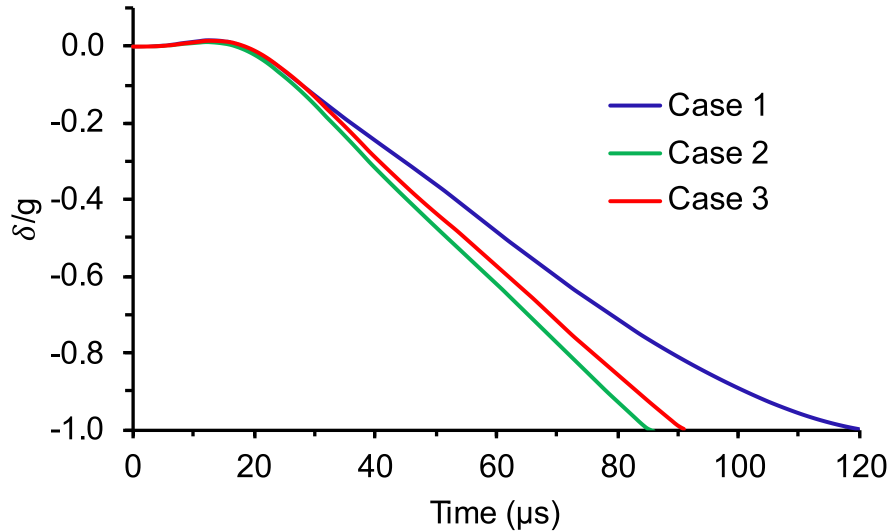

Figure 3.13 Time-dependent response for the three selected designs of the proposed switch.

Further, the von Mises stress in the switch design is critical in determining the RF switch's lifespan. Therefore, to ensure reliable performance, the highest stress in the switch beam during operation must be substantially below the yield stress of the switch material. The yield stress of copper thin films value is varied ranging from 84 MPa to 360 MPa based on various critical factors like grain size, and fabrication techniques [77-79]. Accordingly, we studied the time-dependent von Mises stress in the proposed switch beams during electrostatic actuation, as reported in Fig. 3.14

As seen in the stress plot, the stress grows nonlinearly with time in all cases and reaches a peak of 8 MPa, 11.5 MPa, and 11 MPa for Cases 1, 2, and 3, respectively, when the cantilever is in the actuated state. Essentially, a relatively large anchor area signifies less strain in that location, and hence the maximum stress value for Case 1 is the lowest. In all situations, however, the maximum von Mises stress in the cantilever is less than the yield strength of thin copper films, thus demonstrating a mechanically robust and reliable design. This value is varied ranging from 84 MPa to 360 MPa based on various critical factors like grain size, and fabrication techniques. In our design, the maximum stress which is happened in the anchor is around 8 times lower than the minimum reported yield stress

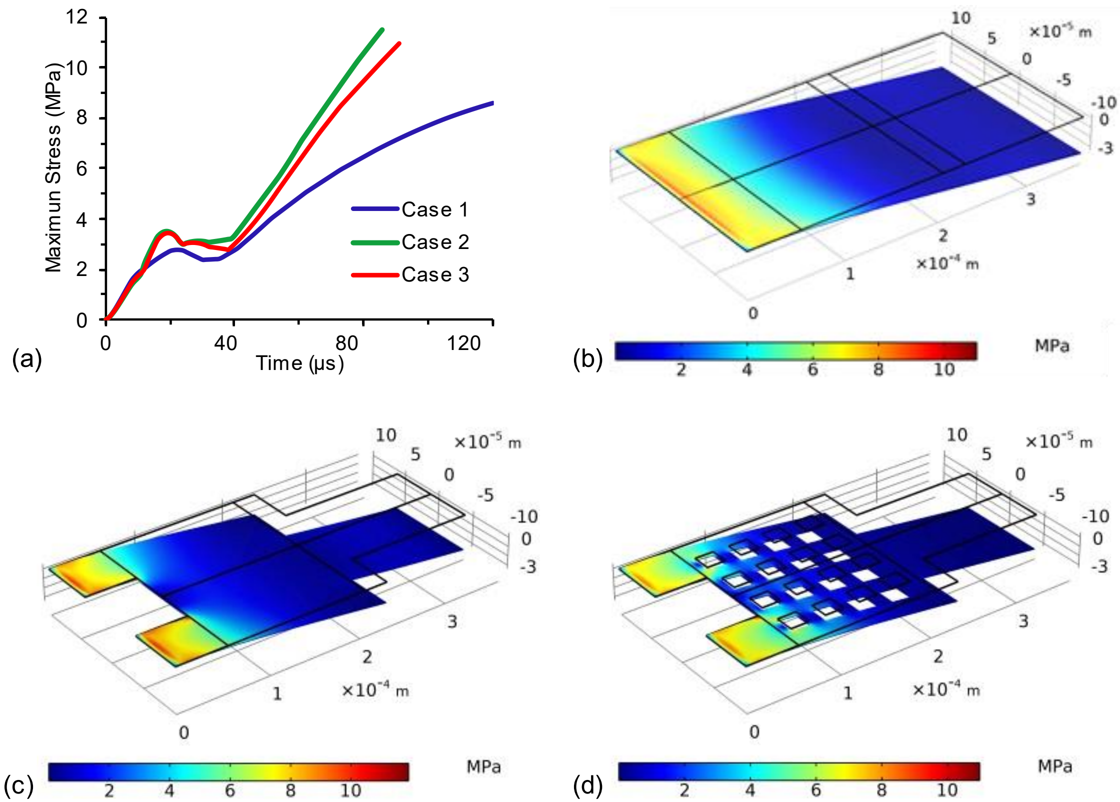

Figure 3.14 (a) Plot of the maximum stress value during actuation for the three cases. Stress contour plots for: (b) Case 1; (c) Case 2, and (d) Case 3.

3.2.3.2. Electromagnetics Analysis

Following the electromechanical analysis, the designed switch geometries were exported to HFSS software (ANSYS Inc., Canonsburg, PA), where the relevant RF characteristics were extracted. Case 2 described in previous sections, was selected among others for the high-frequency analysis, owing to its lowest pull-in voltage value. To conduct a high frequency study on the proposed switch design, a two-port frequency sweep was used, and relevant scattering parameters (*S*-parameters) were extracted. In the absence of actuation voltage, S_{11} and S_{21} reflect the return loss and insertion loss, respectively, whereas S_{21} represents the isolation when the switch is actuated. The capacitance C_{up} influences the switch's return loss and insertion loss and must be maintained to the lowest possible value, while $C_{down\text{-}state}$ defines the switch's isolation and should be as high as possible. Accordingly, the width of the switch's “contact area” was altered in the EM simulations to maximize the switch's RF performance, over a frequency range of 20-60

GHz. The shunt RF-MEMS switch was simulated on glass as well as high resistive silicon (Appendix B).

In the up-state (ON-State), the coupling capacitance predominant the insertion loss, as displayed in Fig. 3.15 for different contact tip widths. At 30 GHz, the switch's insertion loss ranges between -0.065 dB and -0.42 dB as the contact tip width increases from 50 µm to 200 µm. This increase in insertion losses as contact tip width increases is a result of the increasing switch coupling capacitance, that in turn increases insertion losses due to capacitive leakage. Without a doubt, the presented switch design enables effective transmission of RF signals up to 60 GHz while maintaining insertion losses lower than -1 dB.

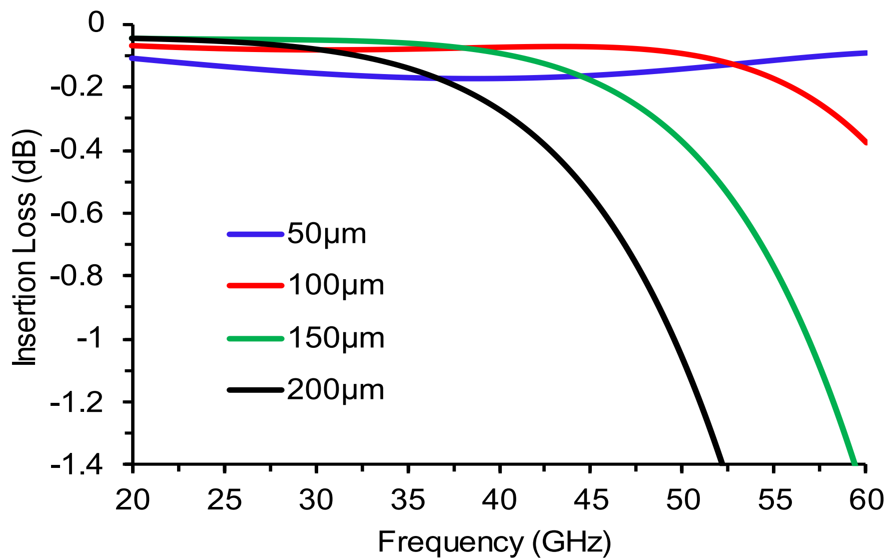

Figure 3.15 Simulated insertion loss against frequency for the proposed switch.

Additionally, the return loss for the switch was found to be -18 dB at the resonance frequency, and -10 dB at 50 GHz.

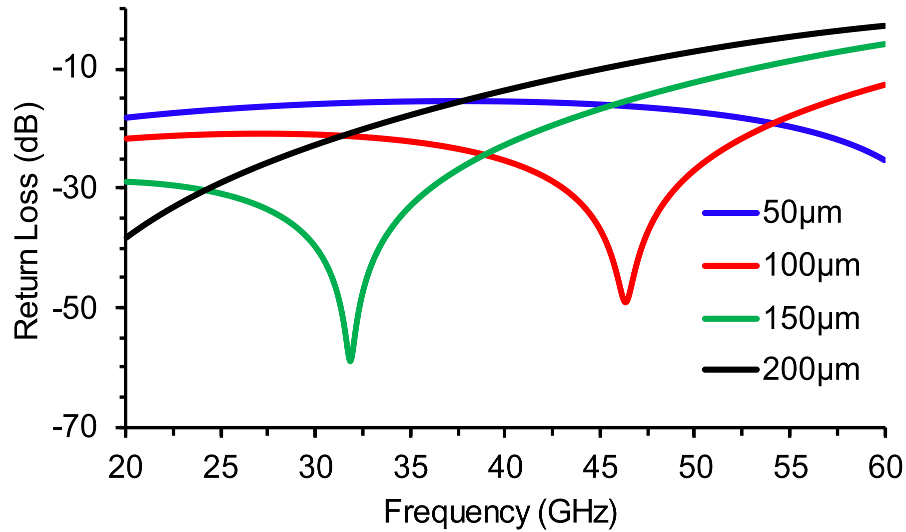

Figure 3.16 Simulated return loss against frequency for the proposed switch.

Likewise, Fig. 3.17 depicts the variation in switch RF isolation values as a function of cantilever contact tip width. The resonance frequency for the switch shifts from 40 GHz to 23GHz when the contact area width rises from 50µm to 200µm, owing to the higher $C_{\text{down-state}}$ associated with increasing contact tip width. Thus, the $C_{\text{down-state}}$ varies causing resonance frequency shift. Among several shunt switch designs with various contact tip width values, a 100µm contact tip width provided us with the highest isolation value of -44.7 dB as well as the lowest insertion loss of -0.14 dB, at 30 GHz.

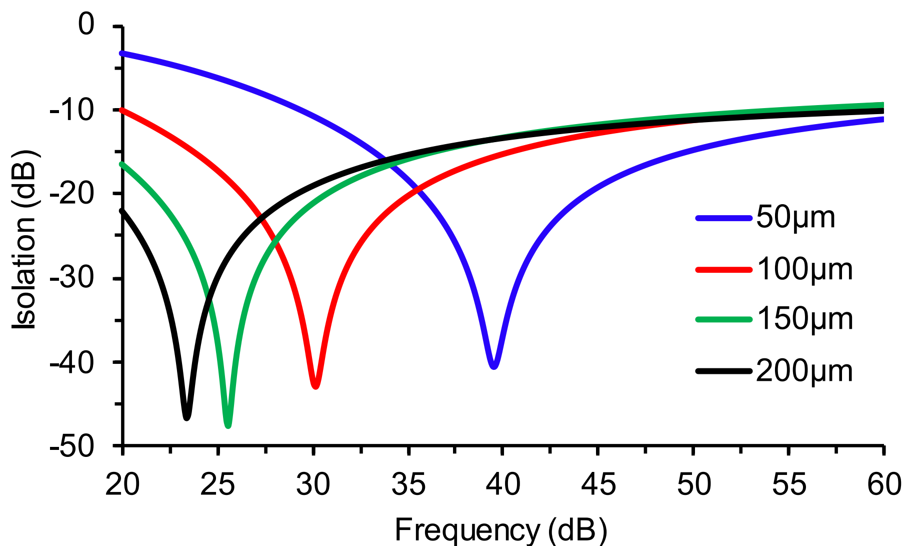

Figure 3.17 Simulated RF isolation against frequency for the proposed switch.

To establish clarity for the study's findings, Table 3.5 compares the suggested switches' performance to that of relevant literature. To summarize, the acquired RF performance results substantially validate the proposed cantilever type shunt switches' efficient functioning in millimeter wave (5G) frequency ranges up to 50 GHz.

Table 3.5 Performance comparison with simulation-based studies in literature

Ref	Pull-in Voltage (V)	Switching Time (μs)	Insertion Loss (dB)	RF Isolation (dB)
[80]	18.3	-	-0.29 @ 35 GHz	-20.5 @ 35 GHz
[81]	3.2	15	-0.01 @ 12 GHz	-44 @ 12 GHz
[82]	4.9	21	-0.8 @ 30 GHz	-50 @ 30 GHz
[83]	4.8	33	-0.25 @ 20 GHz	-20 @ 20 GHz
OUR WORK	9.1	90	-0.14 @ 30 GHz	-44.7 @ 30 GHz

IV. PROCESS FLOW FOR FABRICATION OF CANTILEVER-TYPE RF-MEMS SWITCHES

MEMS fabrication incorporates common complementary metal oxide semiconductor (CMOS) methods such as lithography, chemical vapor deposition (CVD), physical vapor deposition (PVD), epitaxy, oxidation, dry and wet etching, diffusion, and ion implantation. Several of these conventional methods have been adapted for MEMS fabrication, such as the use of thick photoresist, greyscale lithography, or deep reactive ion etching (DRIE). RF-MEMS devices could be followed the standard fabrication processes, which are deposition, lithography, and etching as seen in Fig. 4.1.

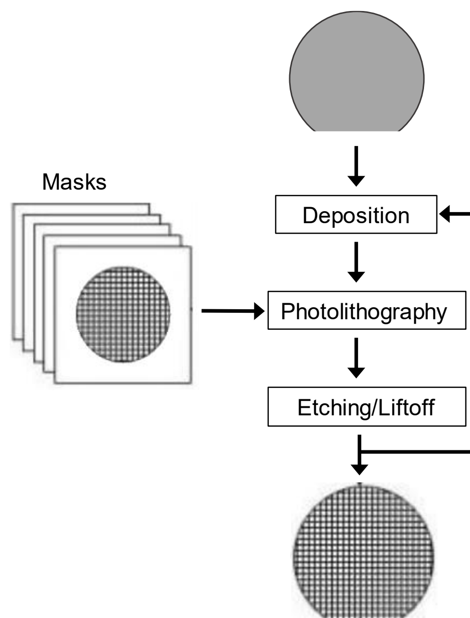

Figure 4.1 Standard MEMS fabrication processes.

In addition, all materials relevant to integrated circuit processing are widely used in the fabrication of RF-MEMS, such as a range of metals and metallic compounds deposited by PVD techniques (Cu, Au, Al, Cr), and also organic materials such as amorphous

silicon, silicon nitride, silicon dioxide deposited by CVD. Where they are usually followed by spin-coating of organic polymer photoresists or thick polyimides and patterned using photolithography technologies. This chapter will detail and analyze each fabrication stage along with the optimized process parameters for both proposed cantilever ohmic RF-MEMS switches designs, discussed in chapter 3. The RF-MEMS switches were fabricated on Borofloat33 glass substrates using standard CMOS technology.

4.1. Overview of the process flow

The fabrication process for this work has been carried out in a standard micromachining process in a Class 100 cleanroom. In brief, the fabrication process for the wavy RF-MEMS switch consists of 7-photolithography mask process. While the shunt RF-MEMS switch followed a very similar process, however, using only a single mask to create the beam (appendix C). The process was carried out in Borofloat33 glass with thickness of 500±10 μm.

First, a polysilicon layer was deposited and patterned using photolithography mask 1 to define the DC actuation electrode and corresponding DC lines, as well as the DC pads for probing (Fig. 4.2b). Followed by a 500nm thick silicon dioxide layer is deposited using PECVD (plasma enhanced chemical vapor deposition) and patterned using mask 2 on top of the DC line, which served as a dielectric layer between the DC electrode and upcoming switch beam layer (Fig. 4.2c). A 1μm thick copper layer was then deposited and patterned using mask 3 to define the CPW line (Fig. 4.2d). At this point, a 200nm thick ZnO sacrificial layer was deposited and patterned to define the anchor point of the switch beam (Fig. 4.2e). A multi-layer thin metallic film stack was then deposited via evaporation and patterned to realize the switch beam, as shown in Fig. 4.2g-f. The multi-layer stack comprises the main copper layer (1 μm thick) shown in Fig. 4.2h, and chromium stressor layers on top and bottom with thicknesses varying from 20 nm - 50 nm, depending on the required bending profile, in Fig. 4.2g and f respectively. Finally, the sacrificial layer was removed, and the switch beams were suspended. Owing to internal stresses, the switch beams self-assembled into bent-up or wavy structures, according to the thicknesses of chromium layers (Fig. 4.2i). The masks for the relevant steps are displayed in Appendix D.

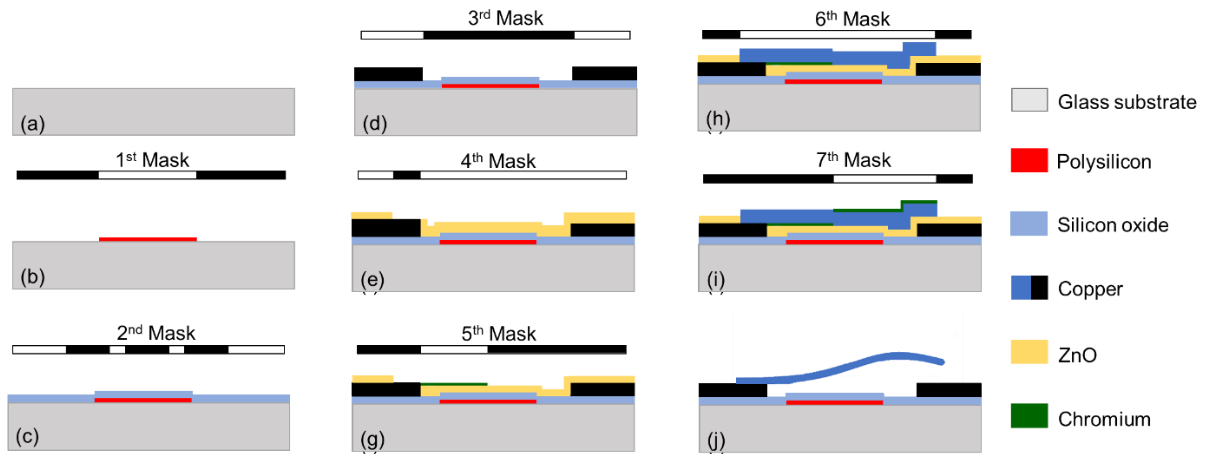

Figure 4.2 The proposed RF-MEMS Switch process flow.

4.2. Cleaning of the Glass Substrate

The first and most vital step in the fabrication flow for both types of RF-MEMS switches is cleaning the glass substrate. The substrates are cleaned subsequent to each wet-chemical treatment by different cleaning techniques for a smoother and less contaminated surface. Firstly, the wafer was left in warm acetone to remove organic contaminations such as grease, oil, or photoresists. If there is no sensitive pattern on the sample, the sample can be placed in an ultrasonic bath for 5 minutes to remove metals and molecular contaminations. Unfortunately, acetone tends to leave its residue on the sample as it evaporates. Therefore, the sample must be placed in an isopropanol (IPA) bath to remove acetone traces, followed by a deionized (DI) water rinse and dried with nitrogen gas (N2). Finally, the sample is backed in oven at 135°C for 10mins to dehydrate leftover $H2O$ molecules.

4.3. Layer 1: Deposition of Polysilicon For DC Bias Line And electrode

Since the transmission line and switch are made of Cu, the actuation electrodes and DC-bias signal lines are ought to be made of high-resistivity doped polysilicon to reduce the coupling with RF lines. That way the bias pads are isolated from the cantilever using thin high-resistivity silicon bias lines.

The deposition of a uniform thin doped polysilicon layer is achieved using sputtering. A thin film of 200 nm of doped polysilicon was deposited in RF (13.56 MHz) magnetron system using a 2-inch diameter target. Initially, pre-sputtering is done for 10 min in order to remove any contamination from the target surface. After pre-sputtering, the target power and argon flow were adjusted to stabilize the deposition rate at 0.4 Å/s for 120 mins.

The first photolithography has been carried out using mask 1 layout to transfer the biasing line and actuation electrode pattern on the wafer, and then dry etched using DRIE using SF_6.

4.4. Layer 2: Deposition Of Silicon Dioxide Intermetal Dielectric Between The DC Bias Line And CPW

The PECVD system was utilized to deposit 500 nm of SiO_2 film, where the wafer is placed in the chamber via load-lock. Before deposition, the chamber is pre-heated for 10 minutes to stabilize the temperature of our sample and then purged with N_2 at a flow rate of 700 sccm for 1 minute. The deposition followed the baseline recipe (table 4.1) at a deposition rate of 70.6 nm/min.

Table 4.1 PECVD Parameters settings

Parameters	Values
SiH4 flow rate	265sccm
NH_3flow rate	1000sccm
N2 flow rate	500sccm
Pressure	1800mTorr
RF Power	140W
LF Power	0W
Temperature	350°C

The second lithography was performed to pattern the dielectric layer by dry etching as it is preferred for obtaining anisotropic profile. The sample was etched using DRIE in a 1.5 min intervals for a total of 7.5 min.

4.5. Layer 3: Metallization To Define The Transmission Line

Lift-off process showed to be the most conventional and ideal way to pattern bi-layer or tri-layer metal with minimum under etching compared to wet etching as shown in Fig 4.3. Firstly, the sample was cleaned with acetone followed by IPA after patterning the oxide layer. Then Hexamethydisilazine (HMDS) was spined on top of the sample for better metal adhesion with the oxide layer. Silane compounds from HMDS promote the chemical adhesion of an organic compound (photoresist) to the non-organic layer. The lift-off techniques require negative wall profile, which is achieved by using AZ 5214E in the image reversal (IR)-mode. The image reversal mode can be reached by activating a specific crosslinking agent in the resist composition. The AZ 5214E data sheet is used to optimize the IR process recipe (appendix E).

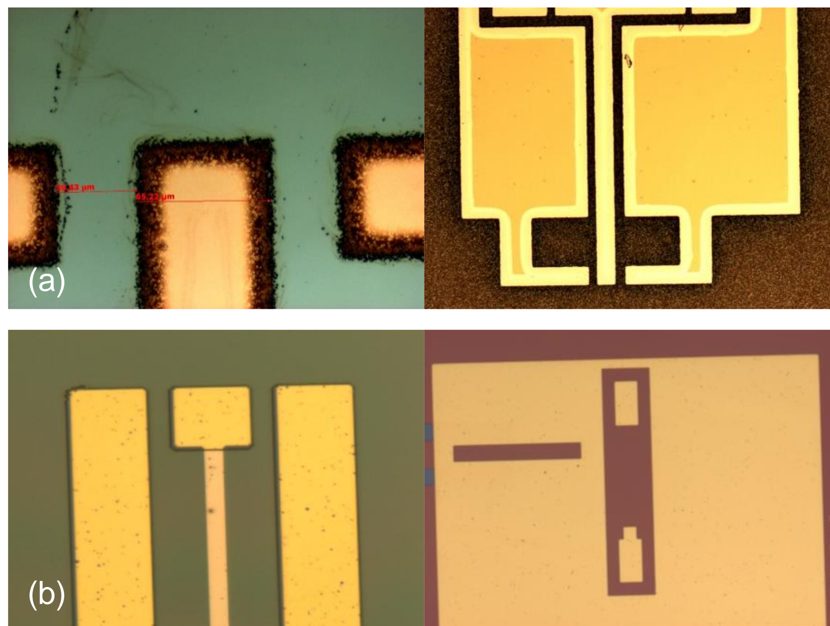

Figure 4.3 Patterning of CPW using (a) wet etching and (b) Liftoff.

After the third photolithography (using mask 3), the deposition of chromium and copper was carried, onto the negative photoresist patterned wafer, by using TORR electron beam evaporator. The graphite crucible pocket was filled with chromium (99.95%) pieces and copper (purity 99.7%) pieces as the source material. The metal deposition procedure was carried out at a base pressure of 5 x 10^{-6} mbar. The power supply was gradually increased by varying current to the tungsten filament until the deposition rate reached the desired

rate and was maintained at 0.6 Å/sec. The coating was carried out for 3 hours. During deposition, the substrate was rotated and maintained at room temperature. A tri-layer Cr/Cu/Cr was deposited to form the CPW, where the first thin layer of 10nm Cr was used as adhesion layer before Cu deposition, while another 5nm of Cr was evaporated on top of Cu to avoid the oxidization of the Cu layer. Finally, the sample was left in acetone for 12hr to remove the AZ5214E and complete the lift-off process.

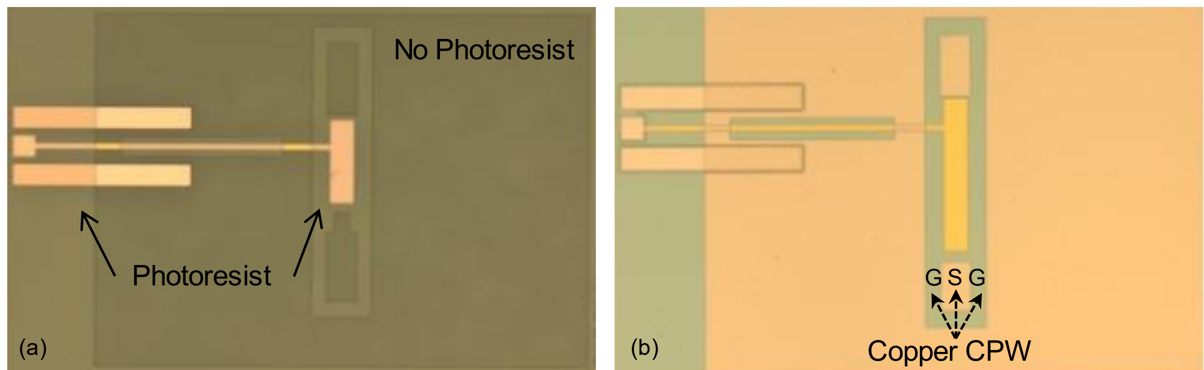

Figure 4.4 Liftoff process (a) After reverse image step before deposition (b) after removing the underneath photoresist.

However, one of the challenges faced during e-beam metal deposition is spitting. Spitting phenomena occurs during the Cu evaporation when liquid droplets are accidentally ejected from the melt pool, resulting in defects in the formed film. These defects severely reduce film yields, causing device failure due to the breakouts of the layer structures. There are many process conditions and parameters, which if left uncontrolled, can have an overwhelming influence on spitting. To begin, the fabrication parameters and factors, include the cleanliness of the evaporation chamber, the uniformity of the crucible liner weight, and the crucible liner material. Once these process variables are maintained consistently, the impact of the Cu source material should be determined. Cu must be exceptionally pure and clean because an organic-free surface results in the least amount of spitting. Finally, during evaporation preheating for degassing the evaporation material or slow heating until it reaches the evaporation point can help reduce spitting [84]. Therefore, the power is applied very slowly until Cu melts into a pool, then the power was gradually increased to achieve desired deposition rate. In addition, the beam location was fixed to further reduce the spitting. Fig. 4.5 shows the before and after the result of the optimized metal deposition.

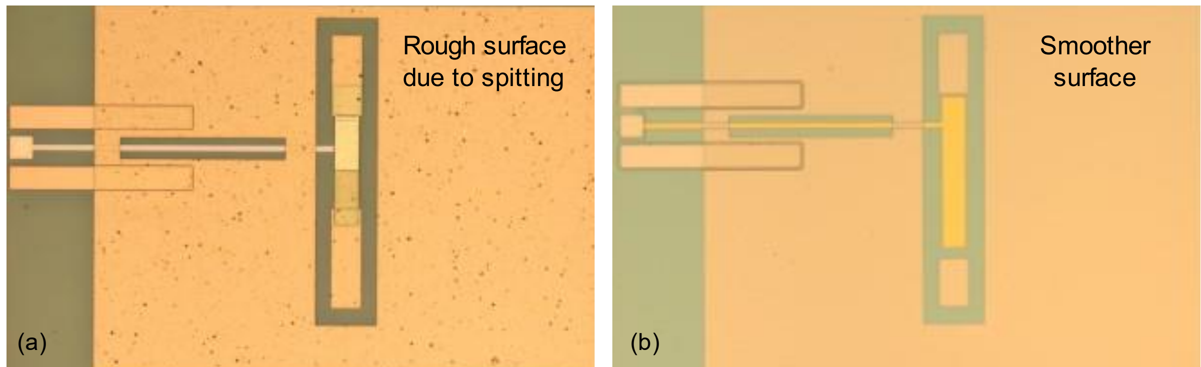

Figure 4.5 The before and after the result of the optimized metal deposition.

4.6. Layer 4: Deposition Of The Sacrificial Layer Deposition And Patterning Of The Beam's Anchor

Sacrificial layer deposition comes after building the CPW, the material used in this layer is critical because it facilitates the formation of the structural layers. Typically, a sacrificial material shall meet certain criteria:

(1) Sufficient mechanical strength to provide a smooth fabrication process.

(2) Adhesive qualities capable of preventing the sacrificial layer from being removed during the fabrication process.

(3) It should exhibit minimum residual stress during fabrication.

Within this thesis we used a wide range of sacrificial layers (i.e. different photoresists, Al_2O_3, Ge, ZnO), among which, ZnO has been selected because of four main reasons: 1) having high selectivity to the other layers at ambient temperatures, 2) being easy to fabricate, 3) having roughly fast etching rate at ambient temperature, and 4) being less hazardous than other acids like Hydrofluoric acid. Table 4.2 summarizes the different materials used as a sacrificial layer in this thesis and their relative difficulties faced.

Table 4.2 Results for different materials used as a sacrificial layer

Material	process	Issue faced	Image corresponded in Fig 4.6
AZ 5214E	Spin coat at 4000rpm hard baked for 12min at 135C and 177 hot plate for 45mun	PR hardened due to evaporation and cracked	a
14% diluted AZ 5214E	Spin coated at 2000rpm baked at 105C and hard baked for 10min at 135C and 177 hot plate for 45mun	PR cracked during deposition, removed using hot acetone and P1316 stripper. Resulted in release related stiction	b, c, d
Al2O3	E-beam evaporation of 300nm thickness	Low selectivity to the other layers	e, f
Ge	Thermal evaporation of 240nm thickness	Beam broke, poor coverage/ conformity can be due to liftoff ears or sharp edges	g
ZnO	RF magnetic sputtering of 200nm thickness	The beam was released successfully	h

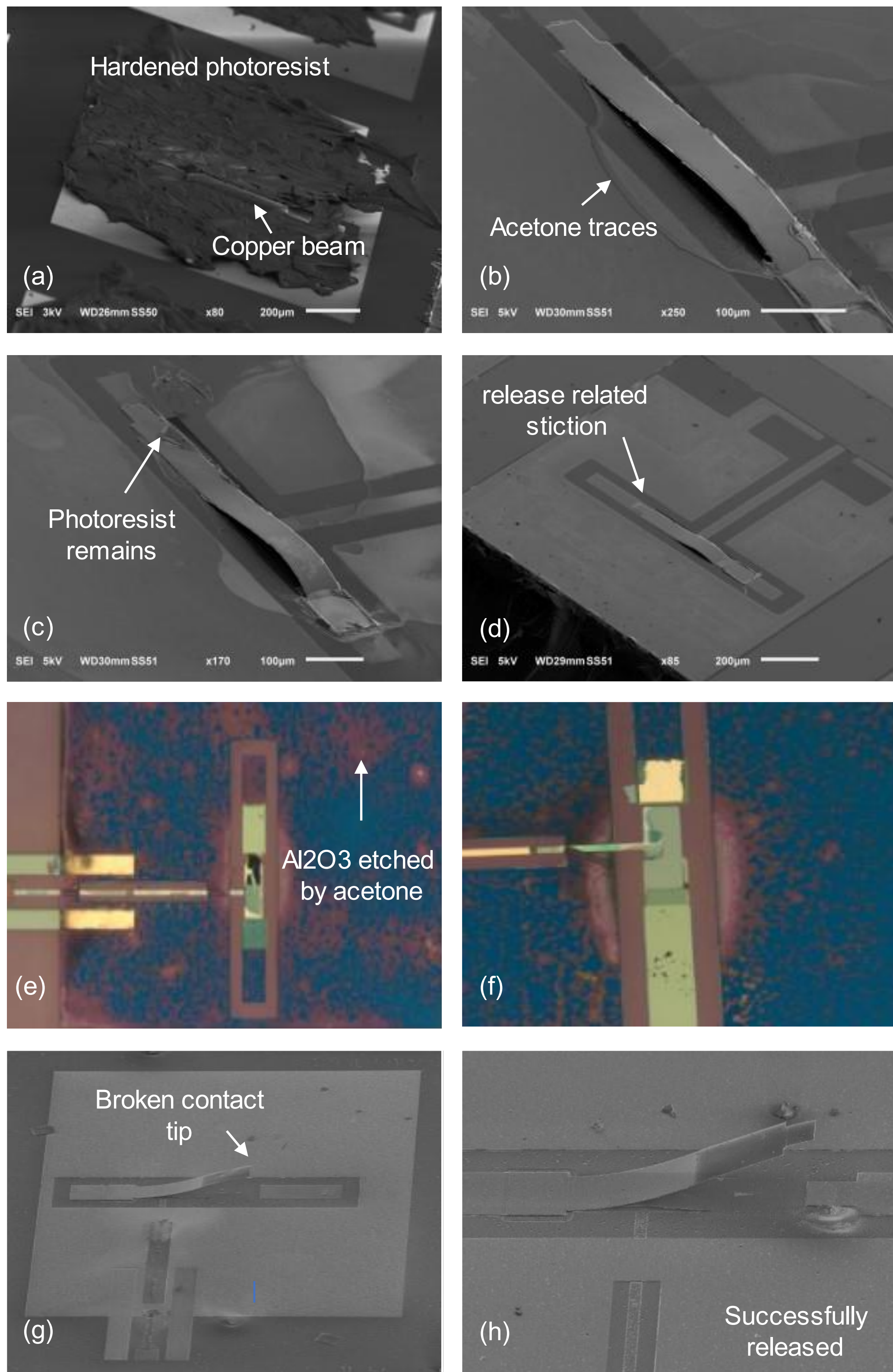

Figure 4.6 SEM and optical images for the results obtained corresponding to different materials used as the sacrificial layer.

Accordingly, Sputter was used to deposit a 200nm ZnO layer. The deposition was carried out using RF (13.56 MHz) magnetron sputtering system using a 2-inch ZnO target. The

sputtering was done in argon-based atmosphere in the pressure range of 14–30 mtorr at 100 W. A pre-sputtering is first performed for 10 min with a pressure control of 30 mTorr and 11.3 sccm gas flow at a power of 50 W. The power is then gradually increased to 100 W for 90 mins at a deposition rate of 0.7-0.8 Å/s. The sputtering process parameters were set as described below.

Table 4.3 Sputtering process parameters

Parameters	**Values**
Method	RF-magnetron
Target	99.99%, 2inch dia.
Sputtering gas	Ar
Max Power	100W
Substrate rotation	5rpm
Target/substrate	5cm

The thin film ZnO deposited on the sample using sputtering provides a conformal step coverage of the structural material layer in the subsequent steps. Following the deposition, the fourth lithography was done to transfer the anchor mask to the sacrificial layer. While there are several ways to etch ZnO (HCl, BHF, HNO3, NH4Cl+NH4OH+H2O, et), one should consider that the etchant used should have a high etching rate to remove the sacrificial layer underneath the cantilever, without affecting the other layers. Thus, a solution of phosphoric acid, acetic acid, and water, with ratio of 1:1:200 was used to etch the ZnO layer.

4.7. Layer 5: Metallization To Form The Cantilever

After patterning of the sacrificial layer, a tri-layer thin metallic film stack was then deposited, for the wavy cantilever switch, thru evaporation and patterned as shown in Fig. 4.7. The cantilever consists of a core Cu layer (1 μm thick), and Cr stressor layers on top and bottom with thicknesses ranging from 20 nm to 50 nm, based on the bending profile desired. Regarding the cantilever-based shunt switch, the beam is made up of a single Cu layer patterned using the 6th mask layout.

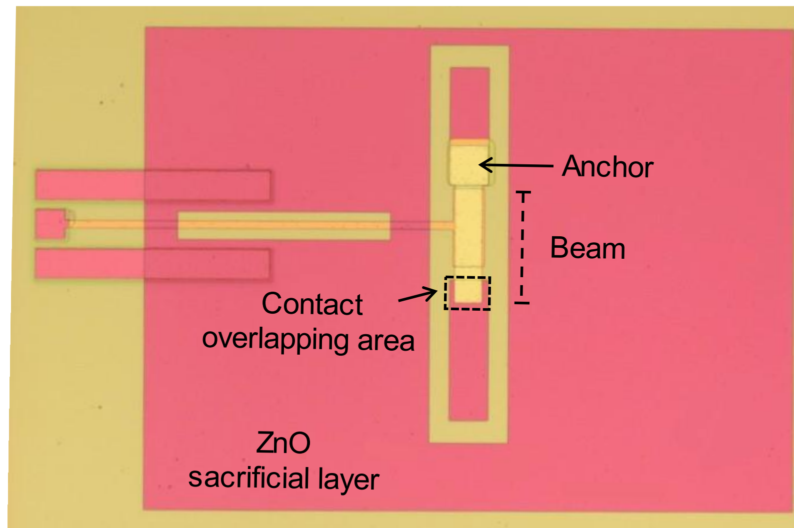

Figure 4.7 Final deposition of the cantilever beam layer.

4.8. Removal of the Sacrificial Layer

The final step in the switch fabrication flow is the etching step to remove the sacrificial layer. The sacrificial layer is removed using a wet etching solution of phosphoric acid, acetic acid, and water, and the switch was successfully released without stiction, as demonstrated in Fig 4,8.

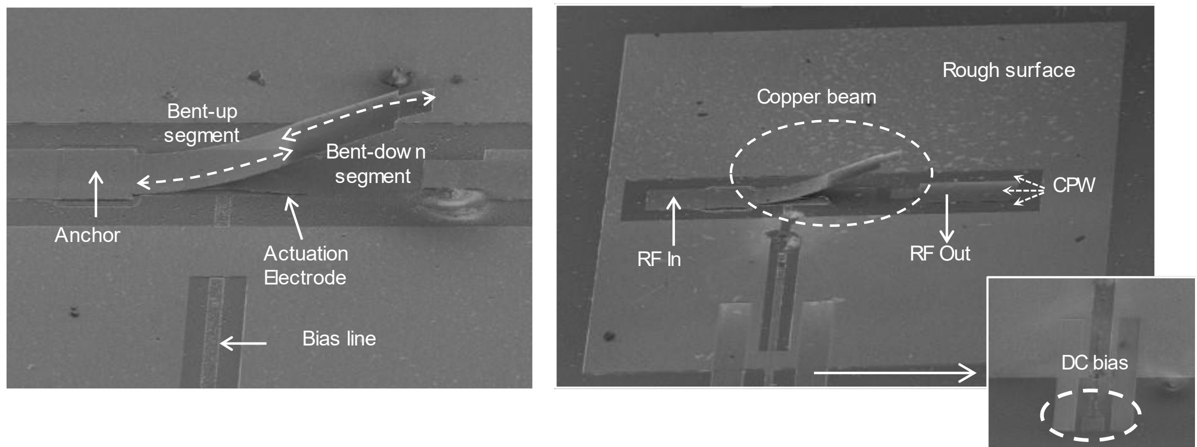

Figure 4.8 SEM images of Wavy MEMS switches.

V. RESULTS AND DISCUSSION

In this chapter, the experimental characterization of the fabrication of cantilever-type RF-MEMS switches were performed according to the electromechanical and electromagnetic characteristics. Accordingly, the S-parameters on the wafer were measured using a two-port network Vector Network Analyzer (VNA) up to 35GHz. While the experimental pull-in curve was performed by applying an external voltage for the switch actuation by a keysight B2900 source measurement unit.

5.1. Wavy Cantilever RF-MEMS Switch Characterization

5.1.1. RF Characterization of the RF Switch

The S-parameters for the RF-MEMS switch were measured by network analyzer using a micro-positioner and ground–signal–ground (GSG) microprobes with 100μm pitch [from GGB Industries]. Before testing, probes calibrations were done using a two-port short-open-load-through method and commercial calibration substrate kit. The RF characteristics in the ON-state and OFF-state were measured. The S-paremter results were extracted from measurements results in Fig. 5.1 of the switch by de-embedding the probe-pad and transmission line parasitic components, In the OFF-state and at high frequency the wavy switch cantilever gave good isolation values (> -20dB) for different switch geometry in a defined frequency range. The proposed design offers additional parameters to tailor the isolation values for the device requirements as a function of the switch capacitance (by controlling the bending profile of the switch as well as overlapping area) and parasitic inductance.

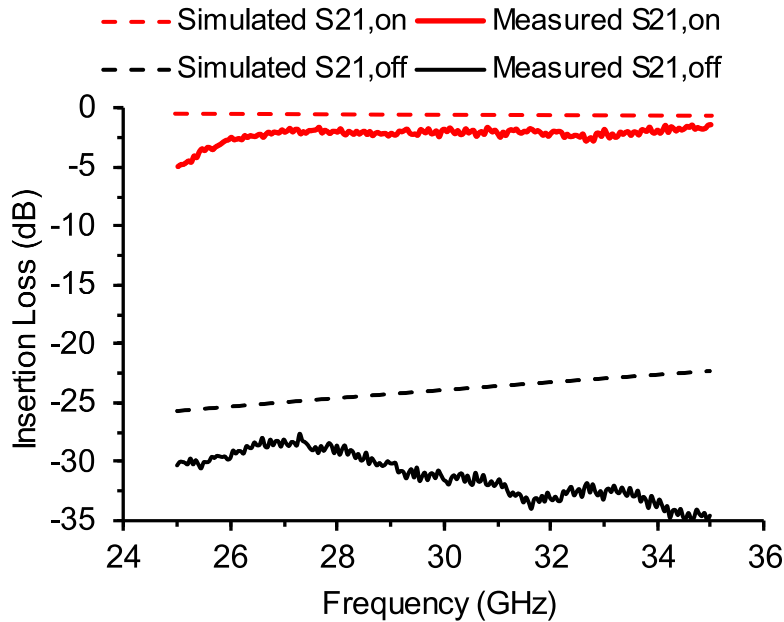

Figure 5.1 Measured S-parameters for the proposed wavy RF-MEMS switch (OFF-state) isolation and (ON-state) insertion loss.

Whereas, in the ON-state, the insertion loss of a CPW without the switch was firstly measured to have approximately -1 dB insertion loss. Therefore, the insertion loss values for loaded CPW with the switch were found to be around -1.5 dB extracted from the thru de-embedding. And through the switch operation analysis we found that the ON-state switch resistance switch is about 70 Ω which is much higher than expected value of 5-10 Ω [5]. This can be due to improper contact of the beam with the RF signal line. The beam tip contacting the RF signal line might suffer from partial contact surface roughness and insufficient contact force, which results in high switch resistance. However, the beam contact area might not be fully in contact with the RF signal line, creating a small air-gap distance between the beam and RF signal line . Consequently, results in a high down-state capacitance, which reduces the insertion losses caused by the high switch resistance.

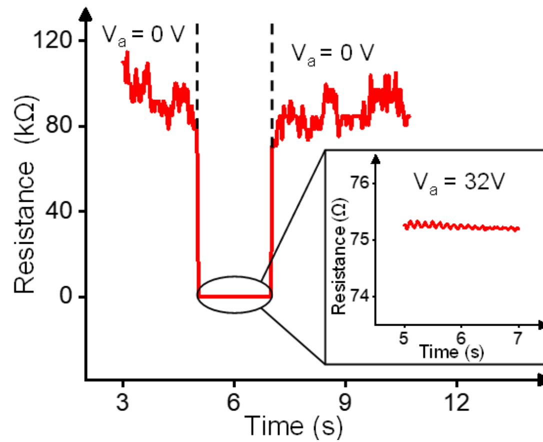

Figure 5.2 On/Off operation performed with fabricated wavy switch.

The measurement results are plotted in Fig. 5.2. The switch performance can be improved through further fabrication optimization and intensive and careful cleaning processes or the use of a smoother material for the contact tip.

5.1.2. Mechanical Characterization of the RF Switch

Electromechanical response of the fabricated switches was measured using tungsten DC probe tips along with the micro-positioners for accurately probing the RF switches. To extract the actuation voltage, the DC actuation electrode was excited with a DC voltage signal through DC pads and DC lines, while a ground signal was supplied to the switch beam. In order to reduce the dielectric charging phenomena, a bipolar DC signal was applied with an AC actuation voltage to avoid charge trapping. The DC voltage setting followed a typical square-wave frequency of 1 kHz, with a transition time of 20 ns. The applied DC voltage was increased in steps and the deflection in the switch beam was observed. For our fabricated switches, the pull-in phenomenon was observed at 32 V (see Fig. 5.2).

VI. CONCLUSION AND FUTURE WORK

Despite the excellent RF performance of electrostatic RF-MEMS switches at mm-wave frequencies, their applicability to practical 5G systems is restricted due to corresponding high actuation voltage requirements, and low reliability as they are more prone to stiction failure. The proposed designs in this thesis tackle these challenges that limit RF-MEMS switches from expanding to high frequency range applications. The thesis is based on the investigation and optimization of cantilever-based RF-MEMS switches in shunt and series configurations.

Utilizing a novel approach based on intrinsic stress-induced self-assembly, a wavy cantilever type RF-MEMS switch with optimized RF isolation and actuation voltage was achieved. The developed switch is distinguished by its low insertion loss and high isolation without sacrificing the pull-in voltage value. Insertion loss values as low as 0.13 dB and RF isolation as high as 28 dB were found while reducing pull-voltage values to less than 41 V (at 30 GHz). Using coupled electromechanical and high frequency simulations, these findings demonstrate the promise of bidirectionally stressed, curved MEMS switches for 5G applications [9]. Moreover, taking into account the tunability of intrinsic stress-induced bending features of cantilevers, the stress gradients in the switch may be adjusted to accommodate varying actuation voltage and isolation levels.

On the other hand, the second design proposed in this thesis demonstrates the use of fixed-free cantilever beams in shunt configuration as RF switches, instead of conventionally utilized fixed-fixed membrane structures, to overcome the voltage constraints. The design is systematically modeled and optimized to achieve high electromechanical response and mechanical reliability. At 30 GHz, the achieved insertion loss and RF isolation values for the proposed switch reach up to -0.065 dB and -46 dB, respectively, thus illustrating a massive potential of proposed cantilever-type shunt switches for 5G applications.

Finally, the proposed designs for RF-MEMS switches were based primarily on fabrication methodologies compatible with CMOS. Chapter 4 covered the fabrication procedure for both RF-MEMS switches using surface micromachined methods compatible with conventional CMOS technology in a clean environment. Each stage of fabrication was thoroughly detailed, and the results were studied in chapter 5.

For future work, the fabrication techniques used can be developed more in order to reduce the common issues such as poor contact quality, current leakage, and further optimization of the cleaning process without affecting the other structural layers. Apart from the fabrication techniques, the devices fabricated in this thesis can be integrated with other building blocks for communication systems such as antennas, or used as filters, phase shifters, etc. In addition, the single RF-MEMS switches can be connected in parallel using a T-junction power divider to construct a Single-Port-Double-Throw (SPDT) switch. This can help to test the materials in real-life systems and can open a wide range of opportunities in applied research, especially in IoT applications and 5g communication systems.

VII. REFERENCE

1. Jungmann, M. and H.F. Schlaak. *Miniaturised electrostatic tactile display with high structural compliance*. in *Proceedings of Eurohaptics*. 2002. Citeseer.
2. Koul, S.K. and S. Dey, *Radio Frequency Micromachined Switches, Switching Networks, and Phase Shifters*. 2019: CRC Press.
3. Liu, A.Q., *RF MEMS Switches and Integrated Switching Circuits*. 2010: Springer US.
4. Rodriguez, J., *Fundamentals of 5G mobile networks*. 2015: John Wiley & Sons.
5. Rebeiz, G.M., *RF MEMS: theory, design, and technology*. 2004: John Wiley & Sons.
6. McFeetors, G. and M. Okoniewski, *Distributed MEMS analog phase shifter with enhanced tuning*. IEEE Microwave and Wireless Components Letters, 2005. **16**(1): p. 34-36.
7. Papapolymerou, J., et al., *Reconfigurable double-stub tuners using MEMS switches for intelligent RF front-ends.* IEEE transactions on microwave theory and techniques, 2003. **51**(1): p. 271-278.
8. Iannacci, J. *RF-MEMS technology: An enabling solution in the transition from 4G-LTE to 5G mobile applications*. in *2017 IEEE SENSORS*. 2017. IEEE.
9. Iannacci, J., *RF-MEMS for high-performance and widely reconfigurable passive components–A review with focus on future telecommunications, Internet of Things (IoT) and 5G applications.* Journal of King Saud University-Science, 2017. **29**(4): p. 436-443.
10. Dubuc, D., K. Grenier, and J. Iannacci, *RF-MEMS for smart communication systems and future 5G applications*, in *Smart Sensors and MEMs*. 2018, Elsevier. p. 499-539.
11. Kim, J.-M., et al., *Electrostatically driven low-voltage micromechanical RF switches using robust single-crystal silicon actuators.* Journal of Micromechanics and Microengineering, 2010. **20**(9): p. 095007.
12. Cho, I.-J., et al., *A low-voltage and low-power RF MEMS series and shunt switches actuated by combination of electromagnetic and electrostatic forces.* IEEE Transactions on Microwave Theory and Techniques, 2005. **53**(7): p. 2450-2457.
13. Lee, H.-C., J.-Y. Park, and J.-U. Bu, *Piezoelectrically actuated RF MEMS DC contact switches with low voltage operation.* IEEE microwave and wireless components letters, 2005. **15**(4): p. 202-204.
14. Shojaei-Asanjan, D., M. Bakri-Kassem, and R.R. Mansour, *Analysis of thermally actuated RF-MEMS switches for power limiter applications.* Journal of Microelectromechanical Systems, 2019. **28**(1): p. 107-113.
15. Ma, L.-Y., et al., *Comprehensive study on RF-MEMS switches used for 5G scenario.* IEEE Access, 2019. **7**: p. 107506-107522.
16. Kumar, R., *A review on RF micro-electro-mechanical-systems (MEMS) switch for radio frequency applications.* Microsystem Technologies, 2021. **27**(7): p. 2525-2542.
17. Oberhammer, J. and G. Stemme, *Low-voltage high-isolation DC-to-RF MEMS switch based on an S-shaped film actuator.* IEEE Transactions on Electron Devices, 2004. **51**(1): p. 149-155.

18. Chen, L., et al., *Contact resistance study of noble metals and alloy films using a scanning probe microscope test station.* Journal of applied physics, 2007. **102**(7): p. 074910.
19. Majumder, S., et al., *Study of contacts in an electrostatically actuated microswitch.* Sensors and Actuators A: Physical, 2001. **93**(1): p. 19-26.
20. Lakshmi Narayana, T., K. Girija Sravani, and K. Srinivasa Rao, *Design and analysis of CPW based shunt capacitive RF MEMS switch.* Cogent Engineering, 2017. **4**(1): p. 1363356.
21. Dutta, S., et al., *Effect of residual stress on RF MEMS switch.* Microsystem technologies, 2011. **17**(12): p. 1739-1745.
22. Jaafar, H., et al., *A comprehensive study on RF MEMS switch.* Microsystem Technologies, 2014. **20**(12): p. 2109-2121.
23. Sharma, T. and A. Tyagi. *Review of mechanical modelling of fixed-fixed beams in RF MEMS switches*. in *2013 Third International Conference on Advanced Computing and Communication Technologies (ACCT)*. 2013. IEEE.
24. Lysenko, I.E., et al., *Analytical approach in the development of RF MEMS switches.* Electronics, 2018. **7**(12): p. 415.
25. Rebeiz, G.M. and J.B. Muldavin, *RF MEMS switches and switch circuits.* IEEE Microwave magazine, 2001. **2**(4): p. 59-71.
26. Ma, L.-Y., A.N. Nordin, and N. Soin, *A novel design of a low-voltage low-loss T-match RF-MEMS capacitive switch.* Microsystem Technologies, 2018. **24**(1): p. 561-574.
27. Fernández-Bolaños Badía, M., E. Buitrago, and A.M. Ionescu, *RF MEMS shunt capacitive switches using AlN compared to Si3N4 dielectric*. 2012, Ieee-Inst Electrical Electronics Engineers Inc.
28. Shekhar, S., K. Vinoy, and G. Ananthasuresh, *Low-voltage high-reliability MEMS switch for millimeter wave 5G applications.* Journal of Micromechanics and Microengineering, 2018. **28**(7): p. 075012.
29. Rangra, K., et al., *Symmetric toggle switch—a new type of rf MEMS switch for telecommunication applications: design and fabrication.* Sensors and Actuators A: Physical, 2005. **123**: p. 505-514.
30. Hah, D. and S. Hong, *A low-voltage actuated micromachined microwave switch using torsion springs and leverage.* IEEE Transactions on Microwave theory and techniques, 2000. **48**(12): p. 2540-2545.
31. Hah, D., E. Yoon, and S. Hong, *A low voltage actuated microelectromechanical switch for RF application.* Japanese Journal of Applied Physics, 2001. **40**(4S): p. 2721.
32. Attaran, A. and R. Rashidzadeh, *Ultra low actuation voltage RF MEMS switch.* Micro and Nano Systems Letters, 2015. **3**(1): p. 1-4.
33. Kuwabara, K., et al. *RF CMOS-MEMS switch with low-voltage operation for single-chip RF LSIs*. in *2006 International Electron Devices Meeting*. 2006. IEEE.
34. Chu, C.-H., et al., *A low actuation voltage electrostatic actuator for RF MEMS switch applications.* Journal of micromechanics and microengineering, 2007. **17**(8): p. 1649.
35. Sharma, P., et al., *Electromagnetic performance of RF NEMS graphene capacitive switches.* IEEE transactions on nanotechnology, 2013. **13**(1): p. 70-79.
36. Blaise, G. and C. Le Gressus. *Charging phenomena, dielectric relaxation processes and breakdown of oxides*. in *Annual Conference on Electrical Insulation and Dielectric Phenomena*. 1990. IEEE.

37. Van Spengen, W.M., et al., *A comprehensive model to predict the charging and reliability of capacitive RF MEMS switches.* Journal of Micromechanics and Microengineering, 2004. **14**(4): p. 514.
38. Zaghloul, U., et al., *Nanoscale characterization of the dielectric charging phenomenon in PECVD silicon nitride thin films with various interfacial structures based on Kelvin probe force microscopy.* Nanotechnology, 2011. **22**(20): p. 205708.
39. Koutsoureli, M., et al., *A study of deposition conditions on charging properties of PECVD silicon nitride films for MEMS capacitive switches.* Microelectronics Reliability, 2014. **54**(9-10): p. 2159-2163.
40. Peng, Z., et al., *Impact of humidity on dielectric charging in RF MEMS capacitive switches.* IEEE microwave and wireless components letters, 2009. **19**(5): p. 299-301.
41. Ya, M.L., N. Soin, and A.N. Nordin. *Theoretical and simulated investigation of dielectric charging effect on a capacitive RF-MEMS switch*. in *2016 IEEE International Conference on Semiconductor Electronics (ICSE)*. 2016. IEEE.
42. Goldsmith, C., et al. *Lifetime characterization of capacitive RF MEMS switches*. in *2001 IEEE MTT-S International Microwave Sympsoium Digest (Cat. No. 01CH37157)*. 2001. IEEE.
43. Parate, O. and N. Gupta, *Material selection for electrostatic microactuators using Ashby approach.* Materials & Design, 2011. **32**(3): p. 1577-1581.
44. Balaraman, D., et al. *Low-cost low actuation voltage copper RF MEMS switches*. in *2002 IEEE MTT-S International Microwave Symposium Digest (Cat. No. 02CH37278)*. 2002. IEEE.
45. Rottenberg, X., et al., *Improved MEMS based shunt switches for telecom applications.* ISWSN'03, 2003.
46. Toscano, L. and E. Long, *CONTROLLING COPPER ROUGHNESS TO ENHANCE SURFACE FINISH PERFORMANCE.*
47. Kumar, R., *Investigations on beam membrane and dielectric materials using Ashby's methodology and their impact on the performance of a MEMS capacitive switch.* Microsystem Technologies, 2021. **27**(12): p. 4269-4289.
48. Saleem, M.M. and H. Nawaz, *A systematic review of reliability issues in RF-MEMS switches.* Micro and Nanosystems, 2019. **11**(1): p. 11-33.
49. Bajwa, R. and M.K. Yapici, *Integrated on-chip transformers: recent progress in the design, layout, modeling and fabrication.* Sensors, 2019. **19**(16): p. 3535.
50. Philippine, M.A., et al., *Topology optimization of stressed capacitive RF MEMS switches.* Journal of microelectromechanical systems, 2012. **22**(1): p. 206-215.
51. Patrikar, R.M., *Modeling and simulation of surface roughness.* Applied Surface Science, 2004. **228**(1-4): p. 213-220.
52. Dastranj, A. and H. Abiri, *Bandwidth enhancement of printed E-shaped slot antennas fed by CPW and microstrip line.* IEEE Transactions on Antennas and Propagation, 2010. **58**(4): p. 1402-1407.
53. Lederer, D. and J.-P. Raskin, *Effective resistivity of fully-processed SOI substrates.* Solid-State Electronics, 2005. **49**(3): p. 491-496.
54. Gamble, H., et al., *Low-loss CPW lines on surface stabilized high-resistivity silicon.* IEEE Microwave and Guided Wave Letters, 1999. **9**(10): p. 395-397.
55. Rothwell, E.J. and M.J. Cloud, *Electromagnetics*. 2018: CRC press.
56. Niessner, M., et al. *Modeling and fast simulation of RF-MEMS switches within standard IC design frameworks*. in *2010 International Conference on Simulation of Semiconductor Processes and Devices*. 2010. IEEE.

57. Iannacci, J., *Practical guide to RF-MEMS*. 2013: John Wiley & Sons.
58. Xu, Y., et al., *A novel RF MEMS switch on frequency reconfigurable antenna application.* Microsystem Technologies, 2018. **24**(9): p. 3833-3841.
59. Bajwa, R., *Intrinsic stress-induced self-assembly of multilayer thin films for fabrication of three-dimensional micro devices*. 2018.
60. Li, J., *Electrostatic zipping actuators and their applications to MEMS*, in *Massachusetts Institute of Technology. Department of Mechanical Engineering*. 2004, Massachusetts Institute of Technology: Massachusetts Institute of Technology.
61. Saleh, H., et al. *Wavy Cantilever RF-MEMS Switch based on Bidirectional Control of Intrinsic Stress*. in *2020 21st International Conference on Thermal, Mechanical and Multi-Physics Simulation and Experiments in Microelectronics and Microsystems (EuroSimE)*. 2020. IEEE.
62. Iannacci, J., *RF-MEMS technology as an enabler of 5G: Low-loss ohmic switch tested up to 110 GHz.* Sensors and Actuators A: Physical, 2018. **279**: p. 624-629.
63. Chu, C.-H., et al., *A low actuation voltage electrostatic actuator for RF MEMS switch applications.* Journal of Micromechanics and Microengineering, 2007. **17**(8): p. 1649-1656.
64. Attar, S.S., Setoodeh, S., Mansour, R. R., & Gupta, D., *Low Temperature Superconducting DC-Contact RF MEMS Switch for Superconducting Tunable Resonators.* IEEE/MTT-S International Microwave Symposium Digest 2012: p. pp. 1-3.
65. Y. Liu, Y.B., X. Liu, *High-Power High-Isolation RF-MEMS Switches With Enhanced Hot-Switching Reliability Using a Shunt Protection Technique.* IEEE Transactions on Microwave Theory and Techniques, , 2017. **65**(9): p. 3188-3199,.
66. Tian, W., P. Li, and L. Yuan, *Research and analysis of MEMS switches in different frequency bands.* Micromachines, 2018. **9**(4): p. 185.
67. Liu, A.-Q., *RF MEMS switches and integrated switching circuits*. Vol. 5. 2010: Springer Science & Business Media.
68. Wei, H., Deng, Z., Guo, X., Wang, Y. and Yang, H., *High on/off capacitance ratio RF MEMS capacitive switches.* Journal of Micromechanics and Microengineering, 2017. **27**(5).
69. Demirel, K., et al., *A folded leg Ka-band RF MEMS shunt switch with amorphous silicon (a-Si) sacrificial layer.* Microsystem Technologies, 2017. **23**(5): p. 1-10.
70. Mafinejad, Y., et al., *Low Actuation Wideband RF MEMS Shunt Capacitive Switch.* Procedia Engineering, 2012. **29**: p. 1292-1297.
71. Kraus, J.D., *Electromagnetics*. 2nd ed ed. McGraw Hill. 1973, New York.
72. Rangra, K., *Electrostatic Low Actuation Voltage RF-MEMS Switches for Telecommunications, Ph. D Thesis.* University of Trento, Italy, 2005.
73. Uvarov, I.V. and A.N. Kupriyanov, *Stiction-protected MEMS switch with low actuation voltage.* Microsystem Technologies, 2019. **25**(8): p. 3243-3251.
74. Mercado, L.L., et al., *Mechanics-based solutions to RF MEMS switch stiction problem.* IEEE Transactions on Components and Packaging Technologies, 2004. **27**(3): p. 560-567.
75. Mercado, L., et al. *A mechanical approach to overcome RF MEMS switch stiction problem*. in *Electronic components and Technology conference*. 2003. Citeseer.
76. Menlomicro, *MM5120 DC – 18 GHz RF SP4T with Integrated Driver*. 2022.
77. Min, H.-G., D.-J. Kang, and J.-H. Park, *Comparison of Tensile and Fatigue Properties of Copper Thin Film Depending on Process Method.* Applied Sciences, 2020. **10**(1): p. 388.

78. Park, J.H., et al., *Tensile and high cycle fatigue test of copper thin film.* Materialwissenschaft und Werkstofftechnik: Entwicklung, Fertigung, Prüfung, Eigenschaften und Anwendungen technischer Werkstoffe, 2008. **39**(2): p. 187-192.
79. Zhang, S., et al., *Mechanical properties of copper thin films used in electronic devices.* Procedia Engineering, 2011. **10**: p. 1497-1502.
80. Li, M., et al., *Design and fabrication of a low insertion loss capacitive RF MEMS switch with novel micro-structures for actuation.* Solid-State Electronics, 2017. **127**: p. 32-37.
81. Sailaja, B. and K.K. Naik, *Design and analysis of serpentine meander asymmetric cantilever RF-MEMS shunt capacitive switch.* Analog Integrated Circuits and Signal Processing, 2020. **102**(3): p. 593-603.
82. Guha, K., et al., *Performance analysis of RF MEMS capacitive switch with non uniform meandering technique.* Microsystem Technologies, 2016. **22**(11): p. 2633-2640.
83. Shekhar, S., K. Vinoy, and G. Ananthasuresh, *Surface-micromachined capacitive RF switches with low actuation voltage and steady contact.* Journal of Microelectromechanical Systems, 2017. **26**(3): p. 643-652.
84. Panjan, P., et al., *Review of Growth Defects in Thin Films Prepared by PVD Techniques.* Coatings, 2020. **10**(5): p. 447.
85. Zhang, P., *Effects of surface roughness on electrical contact, RF heating and field enhancement*. 2012, University of Michigan.

APPENDIX A

RF-MEMS Switch on High Resistive Silicon Substrate Simulations

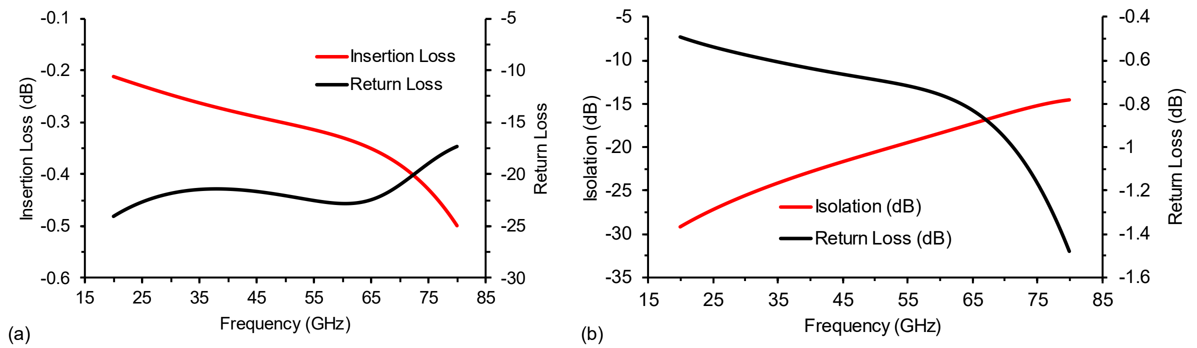

Figure A.1 Simulated S-parameters of wavy RF-MEMS switch on high resistive silicon in the (a) ON-state and (b) OFF-state position.

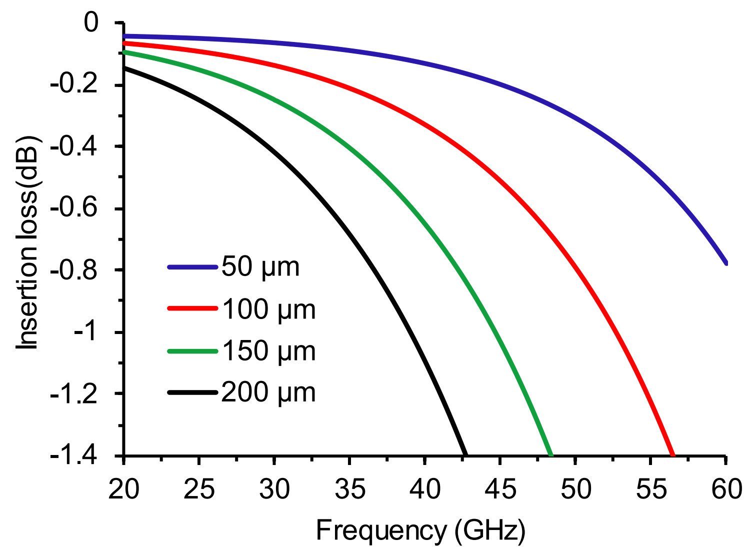

Figure A.2 Simulated insertion loss against frequency for the proposed Cantilever Based Capacitive RF-MEMS Shunt switch on high resistive silicon.

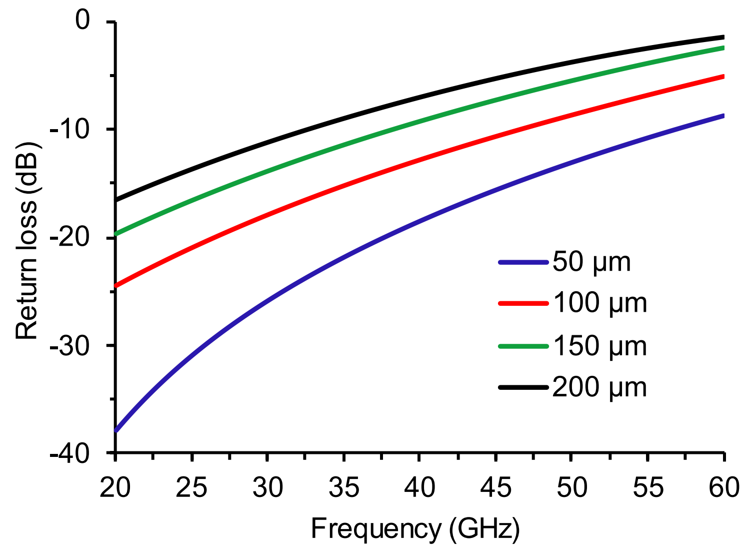

Figure A.3 Simulated return loss against frequency for the proposed Cantilever Based Capacitive RF-MEMS Shunt switch on high resistive silicon.

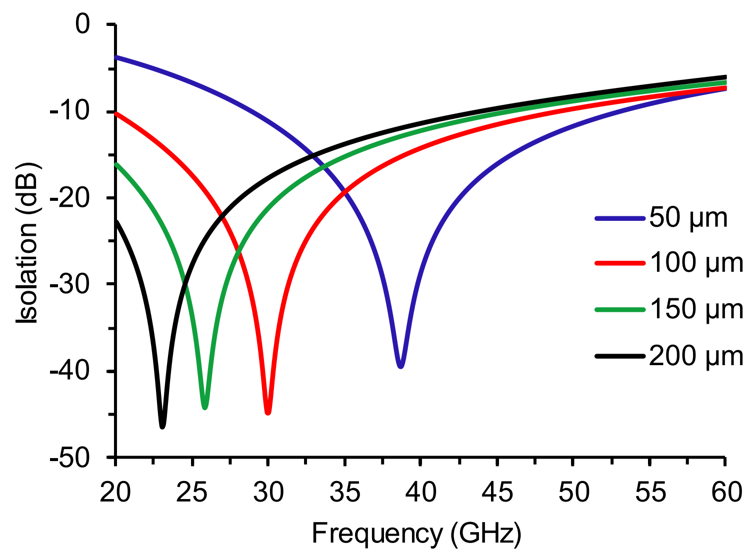

Figure A.4 Simulated isolation against frequency for the proposed Cantilever Based Capacitive RF-MEMS Shunt switch on high resistive silicon.

APPENDIX B

RF-MEMS Switch on Glass Substrate With Copper DC Biasing Electrode Simulations

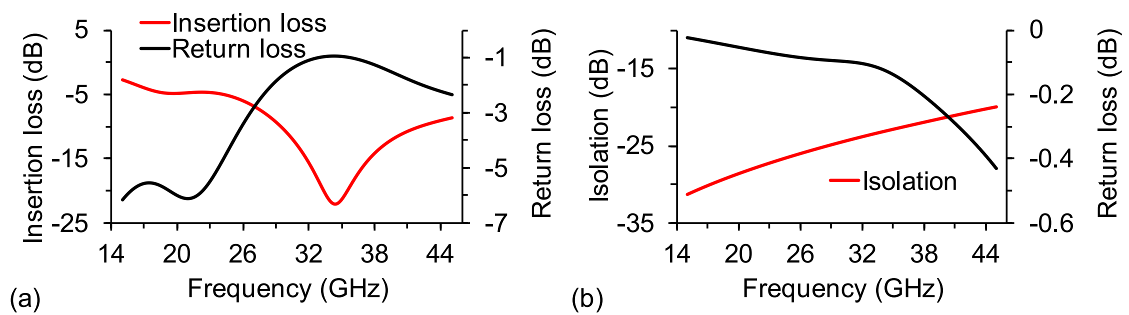

Figure B.1 Simulated S-parameters of wavy RF-MEMS switch on glass substrate using copper biasing electrode in the (a) ON-state and (b) OFF-state position.

Fig B.1 shows the high losses the switch experience using Cu actuation electrode and biasing line in comparison with polysilicon fig. 3.8. Using Cu or gold (Au) or any high conductive metallic bias lines completely alters the signal's behavior as shown above. When the switch's cantilever is actuated, the current surface density increases at the points where the electrode connects to the cantilever, and currents begin to flow on the lines' conducting paths causing undesired resonances. To avoid the effects of the metallic bias lines, one must use high-resistive materials for their bias line and actuation electrodes such as polysilicon or Cr.

APPENDIX C

Cantilever Based Capacitive RF-MEMS Shunt Switch Design process flow fabrication and Results

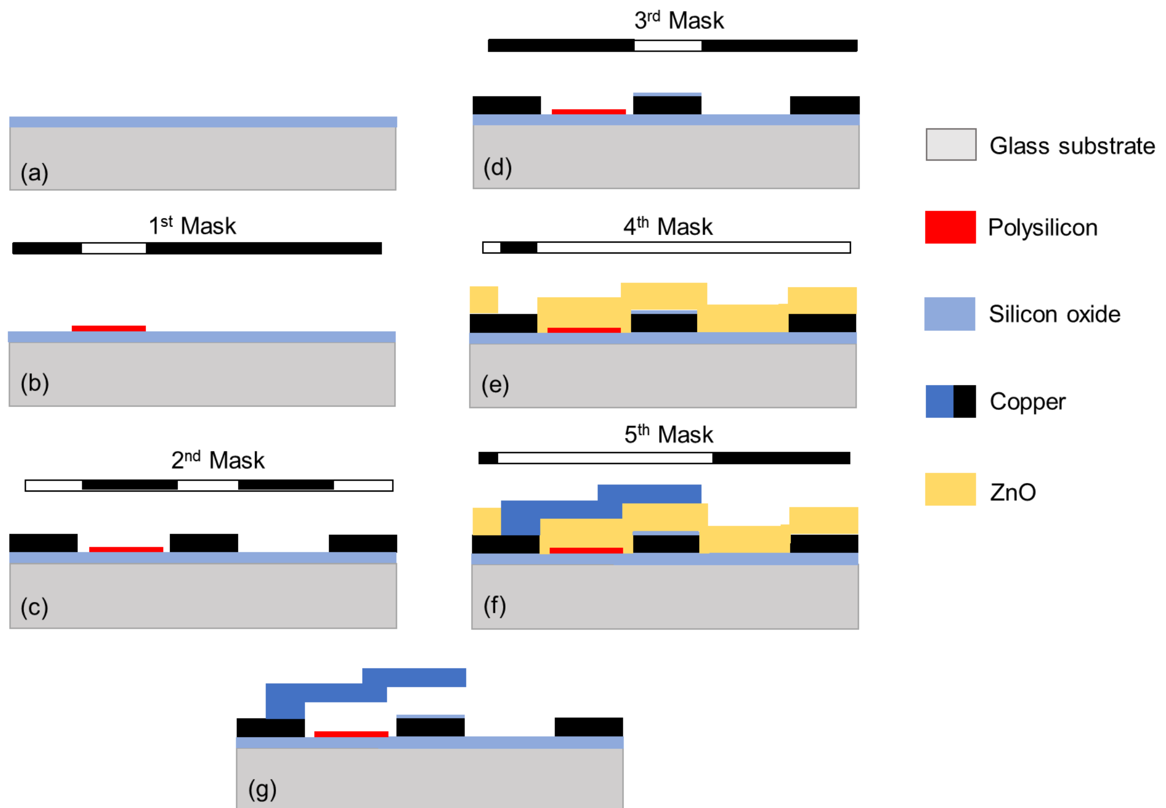

Figure C.1 The proposed cantilever-based capacitive RF-MEMS shunt switch process flow.

In brief, the fabrication process for the cantilever-based capacitive RF-MEMS shunt switch consists of 5-photolithography mask process. The process can be carried on either high resistive silicon or Borofloat33 glass. First, a 500nm thick silicon dioxide layer is deposited using PECVD, followed by the sputtering deposition of the polysilicon layer target. The polysilicon thin film was patterned using photolithography mask 1 to define the DC actuation electrode and corresponding DC lines, as well as the DC pads for probing (Fig. C.1b). A 1 µm thick copper layer was then deposited using e-beam

evaporation and patterned using mask 2 to define the CPW line (Fig. C.1c). In order to create a capacitive contact above the copper central signal line, a thin 200 nm oxide layer was deposited and patterned using mask 3 (Fig. C.1d). At this point, a 4µm thick ZnO sacrificial layer was deposited and patterned (mask 4) to define the anchor point of the switch beam (Fig. C.1e). Finally, mask 5 was used to perform the last photolithography to pattern a 1 µm thick copper layer to construct the cantilever (Fig. C.1f). To release the beam the sacrificial layer was removed, and the switch beams were suspended.

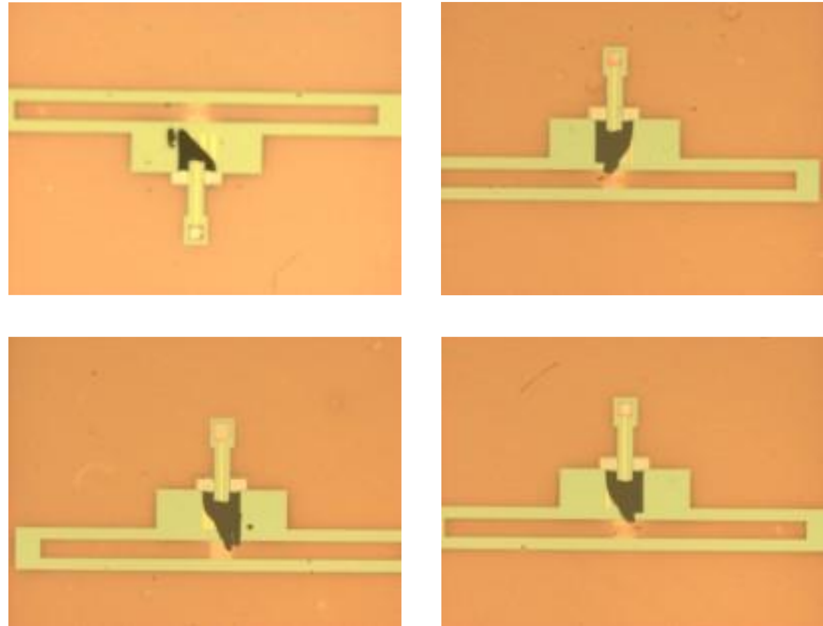

Figure C.2 The deflection of the shunt cantilever RF-MEMS switch.

Fig. C.2 shows the initial results obtained from the fabrication process. Due to the uneven stresses across the non-uniform cantilever beam result in torsion deflect in the beam as shown in fig. C.2. Since the torsional bending causes higher stiffeners in a cantilever than vertical bending. It was challenging to measure the RF and mechanical characterization of the shunt RF-MEMS switch. The switch can be improved by further adjusting the multilayer metal deposition and thicknesses to control the degree of stress

APPENDIX D

Mask layouts used in RF-MEMS Switch Fabrication

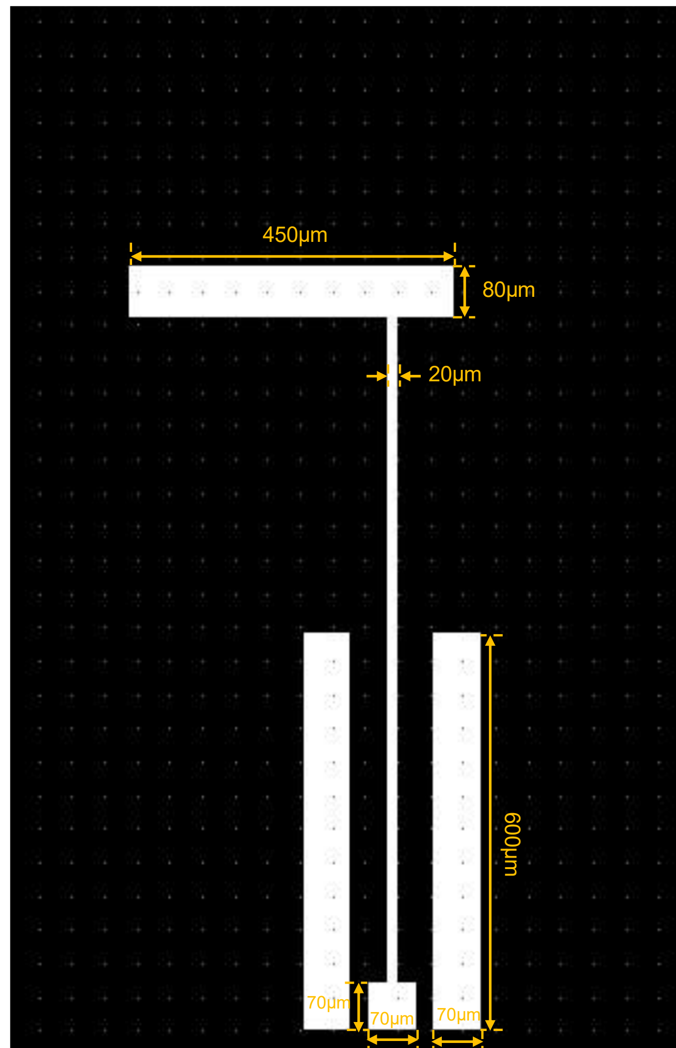

Figure D.1 Mask 1 DC pad and electrode pattern.

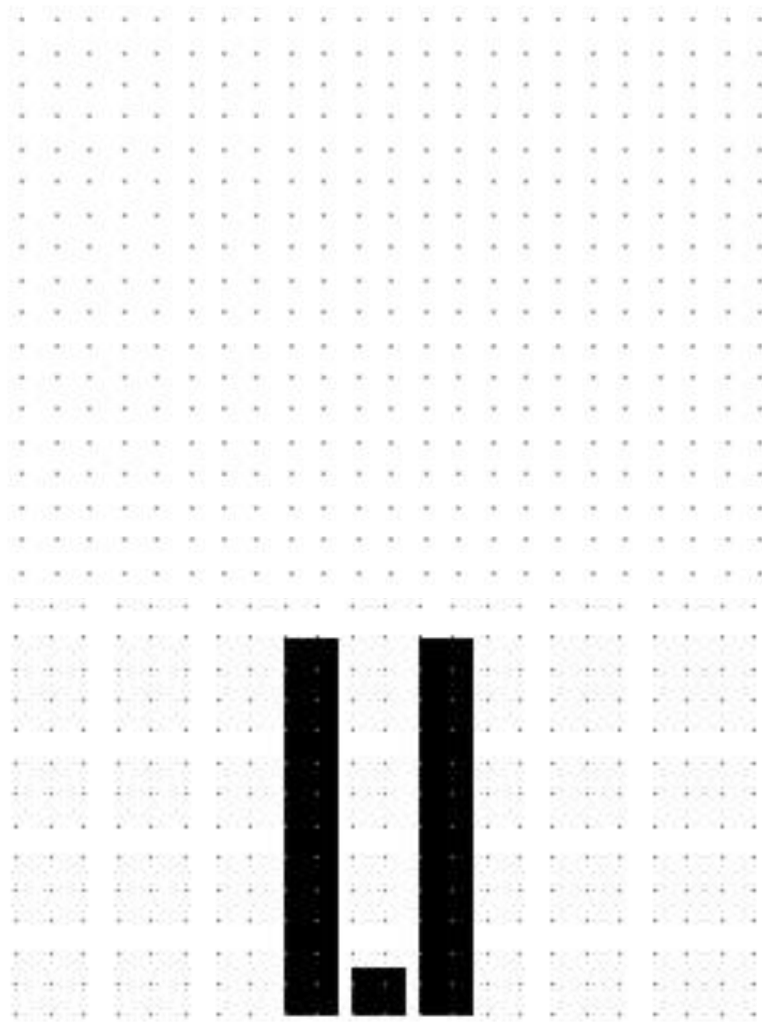

Figure D.2 Mask 2 DC pad pattern to remove oxide layer above DC contact.

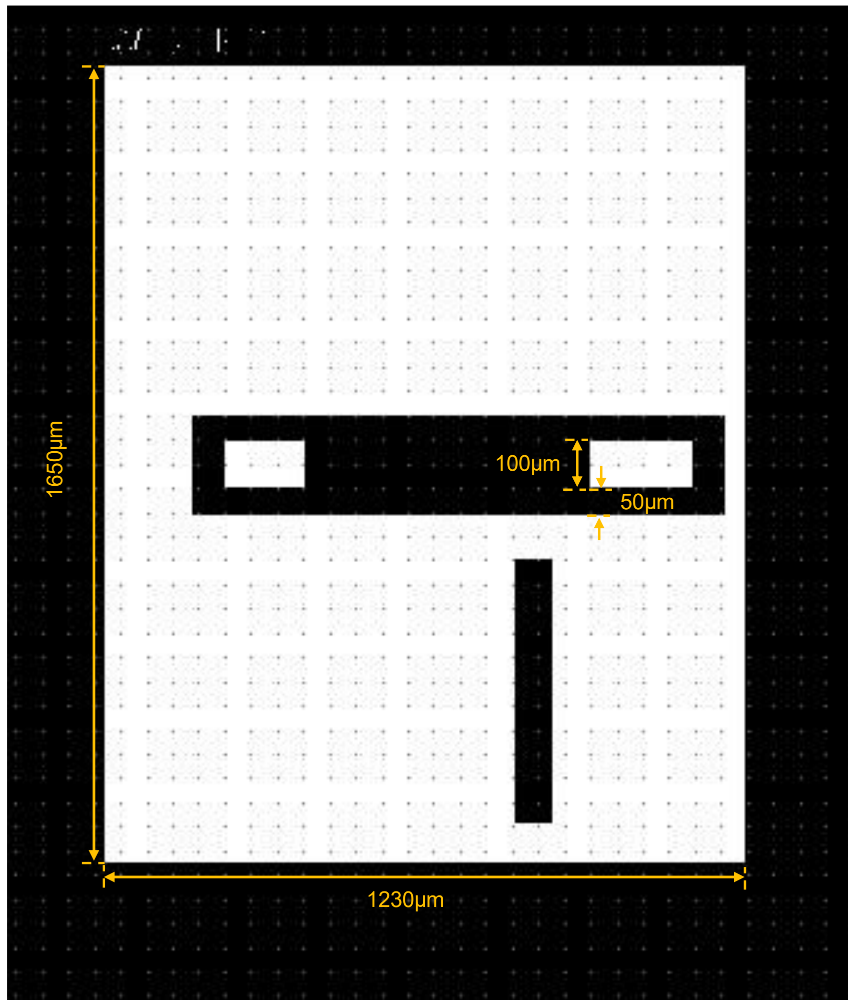

Figure D.3 Mask 3 CPW pattern

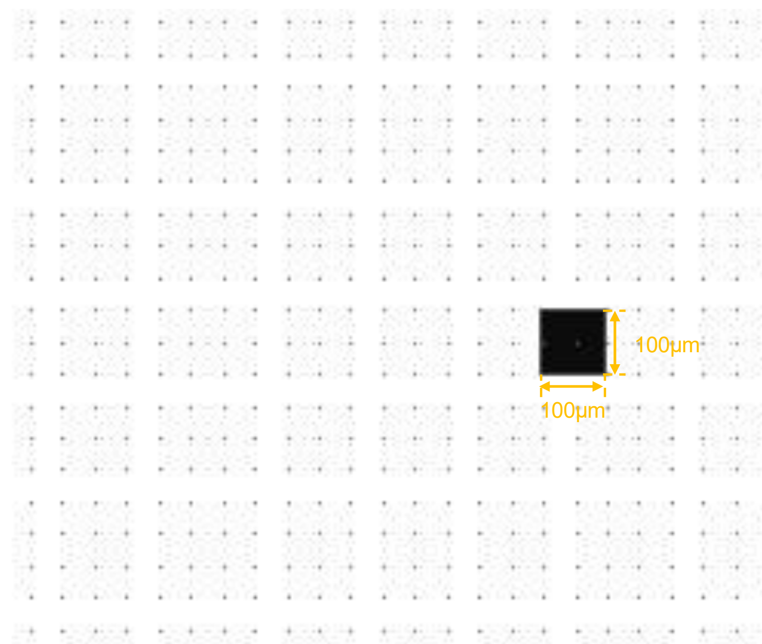

Figure D.4 Mask 4 anchor pattern.

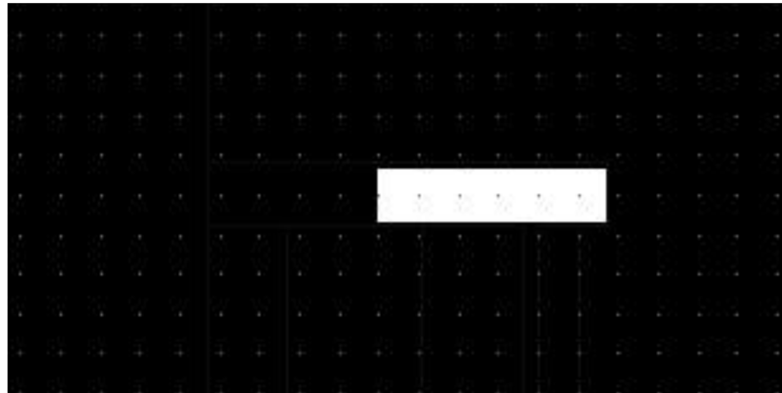

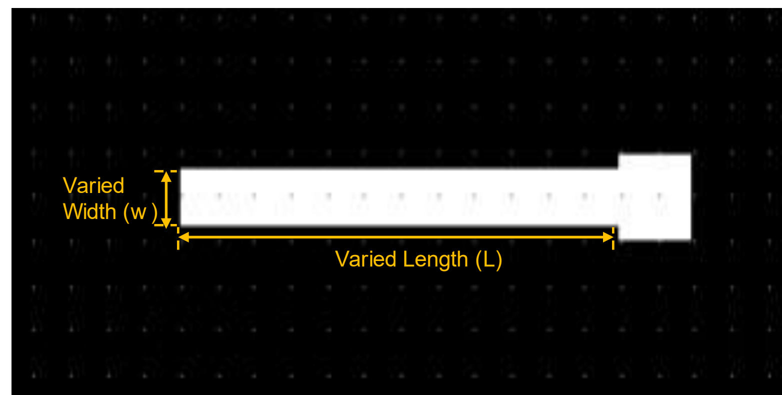

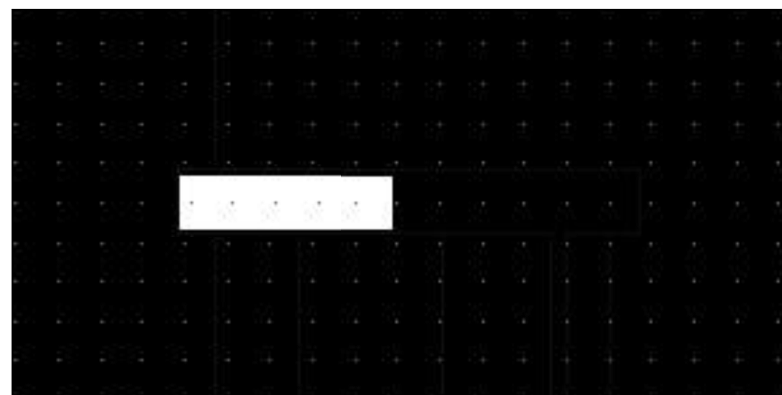

Figure D.5 Mask 5,6 & 7 tri-layer beam patterns.

APPENDIX E

A5214E Photolithography Recipes

Table E.1 Positive photolithography recipe

Spin-coat & Soft-bake Parameters					
Spinning step	Speed	Time	Ramp	Soft bake temperature	Soft bake Time
#1	500 [rpm]	8 [s]	250 [rpm/sec]	-	-
#2	4000 [rpm]	45 [s]	250 [rpm/sec]	110 [°C]	3.5 [min]

Exposure & Development Parameters					
Exposure time	Exposure energy	Mask thickness	Sample Thickness	Developer	Time
5.2 [s]	105 [mJ]	2.37 [mm]	500 [µm]	AZ 726	45 [s]

Table E.2 Image reversal photolithography recipe

Spin-coat & Soft-bake Parameters						
Spinning step	Speed	Time	Ramp	Soft bake temperature	Soft bake Time	Followed by
#1	2000 [rpm]	45 [s]	250 [rpm/sec]	90 [°C]	2 [min]	Exposure #1
#2	2000 [rpm]	45 [s]	250 [rpm/sec]	115 [°C]	2 [min]	Exposure #2

Exposure & Development Parameters						
Exposure step	Exposure time	Exposure energy	Mask thickness	Sample Thickness	Developer	Time

#1	2.8 [s]	56 [mJ]	2.37 [mm]	500 [µm]	-	-
#2	8 [s]	160 [mJ]	No mask	500 [µm]	AZ 726	80 [s]